Environmental Spectroscopy & Biogeochemistry Facility

The Environmental Spectroscopy & Biogeochemistry (ES&B) Facility focuses on environmental molecular science and application of the fundamental concepts of physical chemistry to the study of chemical reactions in heterogeneous natural materials, with an emphasis on soil and subsurface systems. The ES&B Facility staff, along with other Pacific Northwest National Laboratory (PNNL) staff, form a multidisciplinary organization with expertise in chemistry, mineral physics, geochemistry, soil chemistry, microbiology, hydrology, and environmental engineering.

Capabilities are available for materials characterization, aqueous-phase and solid-phase speciation and reaction/kinetic measurements, analytical environmental chemistry, molecular and thermodynamic geochemical process modeling, and large-scale reactive-transport studies. Research includes studies on:

- surface chemistry of Fe and Al oxides, carbonates, and layer silicates
- redox reactions of organic and metal contaminants with Fe- and Mn-containing mineral solids
- biogeochemistry of Fe(III) and Mn(IV) oxide reduction by bacteria and associated biomineralization processes
- mineral surface structure and dynamics by modeling and microscopy
- sorbate surface structure and dynamics on mineral surfaces by spectroscopy
- reactivity and thermodynamics of contaminants at high ionic strengths.

Instrumentation & Capabilities

- Analytical chemistry instrumentation
- Scanning probe microscopy
- Spectrophotometers
- Laser fluorescence microscopy
- Laser spectroscopy and kinetic systems
- Scanning and transmission electronic microscopies
- Laser photoacoustic spectrometer
- Mössbauer spectroscopy
- Electron paramagnetic resonance spectroscopy
- Controlled atmosphere chambers
- Computational geochemical molecular modeling software and hardware
- Hydro- and biogeochemical modeling and software
- Subsurface flow and transport experimental laboratory
- Thermodynamics of aqueous and adsorption reactions

The ES&B Facility consists of seven laboratories that provide specialized capabilities to users from the scientific community. Significant among these capabilities are a Mössbauer spectroscopy facility with variable temperature and conversion electron capabilities; a multi-technique environmental spectroscopy facility with emphasis on optical, vibrational, and photoacoustic spectroscopy; a scanning-probe microscopy facility with emphasis on water-wet mineral and mineral-microbe systems; and computational geochemistry molecular modeling expertise and software for various mineral and chemical systems, including layer lattice silicates, oxides, and bacterial surfaces.

These laboratories, which are described below, are located proximately to facilitate multi-technique studies. Environmental chambers are available with spectroscopic access to

allow controlled-atmosphere experiments. These laboratories are located near other instrumentation integral to environmental molecular science, including high-resolution scanning and transmission electron microscopies and a variety of ultra-high vacuum microprobe techniques for surface analyses.

Optical Spectroscopy Laboratory. Laser-based fluorescence, nonlinear, photoacoustic, and Raman spectroscopies are available to use in investigations of aqueous and interfacial reactions. Kinetic studies ranging from stopped-flow to ultra-fast optical pump-probe methods can be performed. Cryogenic capabilities for enhanced spectroscopic studies of heterogeneous materials are available. Specially designed sample cells allow high-pressure and high-temperature studies, as well as spectroscopic studies of particle suspensions.

Infrared Spectroscopy Laboratory. State-of-science Fourier-transform (FT) spectrometers enable the study of various mineral-chemistry topics as well as sorbate binding mechanisms at mineral, biotic, and organic interfaces. The modular design of the spectrometers in this laboratory enables rapid changing of detector and beam-splitter combinations, so researchers can readily change from the visible (400 to 700 nm) to the near- (770 nm to 2.5 μm), mid- (2.5 to 25 μm), or far-IR (25 to 1000 μm) ranges of the light spectrum. A vacuum bench equipped with a helium-cooled bolometer and step-scanning capabilities is optimized for far-infrared measurements down to 10 cm^{-1} as well as time-resolved spectroscopy at 10 ns resolution. A nitrogen-purged system equipped with a microscope and temperature-controlled mapping stage (-200 to 600°C) allows spatially resolved infrared measurements at the 60-μm level. A variety of cells are available for analyzing gas, liquid, solid, and slurry samples using a variety of techniques including attenuated total reflectance, diffuse reflectance (DRIFTS), specular reflectance, gas sampling, liquid transmission, solid transmission, and a photoacoustic cell and detector. Raman vibrational analyses can be obtained using the FT-Raman module and Raman microscope.

Mössbauer and Electron Paramagnetic Resonance (EPR) Spectroscopy Laboratory. Mössbauer spectrometers with cryogenic capabilities allow studies of Fe structure and redox chemistry in oxides, clays, and biogeochemical systems. Software incorporating Voigt-line fitting and quadrupole-splitting distributions enable state-of-science spectral deconvolution and fitting. A continuous-wave multi-frequency (S, X, and Q bands) EPR spectrometer equipped with He-cooled cryostats and a stop-flow-freeze quench system allows studies of free-radical reactions and electronic environments of paramagnetic species in solids and suspensions and at surfaces.

Imaging Microscopy Laboratory. Optical and scanning-probe microscopies are available for particle imaging from millimeter to nanometer scales. A laser confocal microscope that allows three-dimensional imaging is linked to optical spectroscopy systems. A state-of-science scanning-probe microscopy facility has been developed for imaging water-wet samples, microbe-water, and mineral-microbe interfaces, and for characterizing a wide variety of environmental materials.

Environmental Analytical Chemistry Laboratory. A wide variety of instrumentation is available for quantification of inorganic and organic contaminants and their reaction, transformation, or degradation products. State-of-science separation instruments, including gas and high-performance liquid chromatographs as well as capillary electrophoretic

separators coupled with mass spectrometry are available to users engaged in diverse research activities. An inductively coupled plasma mass spectrometer with laser ablation for solids analysis and a collision cell for improved detection of oxide interfering elements (e.g., Fe) is available for broad-spectrum, high-sensitivity inorganic analyses.

Computational Geochemistry Laboratory. A graphics, simulation, and modeling laboratory, with multiple workstations linked to the computational infrastructure of EMSL, supports research in the ES&B Facility. This laboratory is equipped to perform molecular dynamics and electronic structure calculations as either a stand-alone activity or in support of experimental or spectroscopic measurements. Thermodynamic and kinetic geochemical codes also are available to the user, as are multidimensional geochemical reaction/transport codes for numerical experiments or simulation of the intermediate-scale flow and transport experiments described below.

Subsurface Flow and Transport Experimental Laboratory. This new laboratory is equipped for intermediate-scale (i.e., meter-scale) experimentation in single- and multi-fluid (air-water, air-nonaqueous phase liquid [NAPL]-water, NAPL-water) porous media systems. These unique experimental systems allow testing of basic theories of flow and transport; studies of coupled processes involved with microbial, reactive chemical, or colloid transport; and experimental simulation of subsurface remediation scenarios. Close linkages exist between this center and the modeling facility, as pre-and post-experiment modeling are key to experimental design and interpretation.

Upgrades

The "Seattle" computer cluster was upgraded with six additional nodes (12 processors), an 85% increase. This upgrade allows a significantly higher throughput for users' geochemistry molecular modeling calculations.

The Subsurface Flow and Transport Experimental Laboratory has been established for intermediate-scale (i.e., meter-scale) experimentation in single- and multi-fluid (air-water, air-nonaqueous phase liquid-water, nonaqueous phase liquid-water) porous media systems. The primary advantage of intermediate-scale experiments is that field-scale processes can be mimicked under controlled conditions. Design and construction of the laboratory's core capabilities, a dual-energy gamma radiation system, and an intermediate-scale flow cell have been completed. These capabilities will be used to nondestructively and nonintrusively determine fluid saturation, porous medium bulk density, porosity, and salt concentration values.

Another capability for the Subsurface Flow and Transport Experimental Laboratory, an automated saturation pressure apparatus to simultaneously determine fluid pressures, saturations, and flow rates of soil cores, has been designed, constructed, and tested. Saturation-pressure relations are the cornerstone of numerical subsurface flow modeling of the vadose zone or other multi-fluid systems.

A closed-cycle refrigeration (CCR) cryostat was purchased and installed for low-temperature Mössbauer spectroscopy measurements. Previously low-temperature experiments could be performed only at 77 K and 4.2 K using an open-cycle cryostat that had poor hold times of the liquid nitrogen and liquid helium, which could cause instability issues. With the CCR cryostat, temperature stability can be achieved at any temperature for indefinite time periods, which will improve data collection efficiency, lower costs associated with liquid nitrogen and liquid helium procurement, and eliminate labor costs associated with recharging the cryostat.

The confocal microscope system was upgraded to a Nikon TE-2000 optical microscope with Acton-Research MicroSpec-2150i spectrograph. This new system, along with the existing Roper scientific intensified charge coupled device camera system, will add an enhanced coupling efficiency to the existing laser systems, as well as improved stray-light rejection. The system combines imaging capabilities with high spectral resolution and high throughput for a variety of applications ranging from routine optical imaging of materials, soils, clay minerals, and microorganisms, to time-resolved fluorescence imaging of uranium-contaminated sediments and metal uptake in biological systems such as plants and microbes.

An Ultra Lasertech 8822 CO_2 Laser was installed. The new laser is line tunable using an intracavity grating for wavelength selection between 9.2 and 10.9 microns with a maximum 15 W power output.

Molecular Templating for Highly Selective Detection of Relatively Small Molecules

RS Addleman,[(a)] GE Fryxell,[(a)] JT Bays,[(b)] ED Bott,[(c)] Z Wang,[(a)] and PL Gassman[(d)]

(a) Pacific Northwest National Laboratory, Richland, Washington
(b) United States Military Academy, West Point, New York
(c) Whitman College, Walla Walla, Washington
(d) W.R. Wiley Environmental Molecular Sciences Laboratory, Richland, Washington

Molecular templating using a mesoporous support promises to provide a highly selective, robust, and reliable method of detecting specific, relatively small molecules from among many interfering species. Interest in this area has burgeoned in the past two years with increasing concern about the early detection of chemical agents or unexploded ordinance (UXO). Ideally, the presence of these compounds would be detected at a trace level with 100% specificity to minimize exposure and the potential for false-positive responses.

Previous and ongoing work has focused on the creation and functionalization of a high-surface-area silica layer (mesoporous silica) bound to a silicon substrate. Mesoporous materials with a surface area of approximately 1000 m^2/g covered with a variety of monolayer coatings are now readily available. The self-assembled monolayer (SAM) consists of functional groups tethered to the silicon surface to form a self-assembled monolayer on a mesoporous support (SAMMS). Functional groups are chosen for their ability to directly bind with either a molecule of interest, or to coordinate to lanthanide ions to which a molecule of interest may bind. The molecule of interest may then be templated, as shown schematically in Figure 1, to give "lock-and-key" selectivity. Analyte detection may then be accomplished through a variety of methods.

The recent availability of functionalized mesoporous materials means that the activity of a monolayer contained within a mesoporous support remains virtually unexplored [steps (b) through (f) in Figure 1]. In this study, we examined the chemical activity of two SAMS contained within a mesoporous film.

While several different functional groups were available to us, we focused on samples functionalized with acetylphosphonate and with trimethoxybenzene. These functional groups were selected because of their different binding modes with molecules of interest. The acetylphosphonate functional group is expected to bind to a lanthanide, either europium or terbium, which may in turn coordinate any of several Lewis base molecules of interest, as shown in Figure 1. The

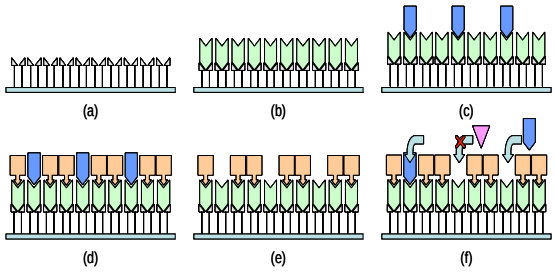

Figure 1. Description of the sequence necessary to create a highly specific molecular template. (a) SAM covering substrate. (b) Lanthanide ions are then loaded onto some of the functional groups located at the end of one or more SAM monomer(s). (c) The analyte of interest binds to the lanthanide via a Lewis acid-base interaction. (d) After analyte loading, the remaining sites are occupied by molecules that serve to fill in the sites around the analyte. (e) The analyte is then chemically stripped from the surface, leaving behind holes selectively patterned by the filler molecules to fit the analyte. (f) Now only the analyte may bind to sites on the surface in a "lock-and-key" manner; other molecules will not fit in the active sites patterned for the analyte.

trimethoxybenzene functional group is expected to interact by pi-stacking with aromatic molecules, such as those found in TNT (trinitrotoluene) or picric acid (trinitrophenol).

For the SAMMS with acetylphosphonate (Ac-Phos) functional groups, we examined europium uptake of the mesoporous material (Figure 1b). After exposing silicon wafers with a 1.7-micron-thick mesoporous layer coated with the Ac-Phos SAMMS to solutions of varying europium concentration, we obtained fluorescence excitation and emission spectra for each of the samples. We were able to observe emission spectra by exciting the narrow europium absorption bands, and by exciting broader bands that result from the SAMMS substrate. Emission spectra displayed three prominent emission bands and several minor bands that varied in proportion to europium loading. These spectra confirmed several properties of the SAMMS that were studied: 1) SAMMS are transparent to ultraviolet and visible light; despite electron micrograph images showing an oriented grain to the SAMMS surface; 2) there appears to be no polarization of reflected light; and 3) the strength of emissions spectra were proportional to europium loading. Europium loading levels for the SAMMS were quantified by examining each solid sample using x-ray photoelectron spectroscopy and by examining the remaining europium concentration of each solution used to load the SAMMS by inductively coupled plasma. These techniques have provided unambiguous and mutually supporting information that allows us to quantify europium uptake on the SAMMS. Interpretation of the fluorescence spectra shows the complexity of the interactions between the europium and the SAMMS. Further experiments using time-resolved, laser-induced fluorescence to examine the expected variation of europium fluorescence lifetime with increased europium loading will allow for a more thorough characterization of how europium binds in the SAMMS.

SAMMS functionalized with 1,2,3-trimethoxybenzene were also examined using fluorescence spectroscopy. Broad excitation and emission bands were observed, similar to those expected for a solution spectrum of an aromatic compound. Both nano- and picosecond time-resolved, laser-induced fluorescence spectra of trimethoxybenzene SAMMS and trimethoxybenzene SAMMS exposed to several test materials (benzene, naphthalene, toluene, and nitrotoluene) produced traces that show multiple decay pathways rather than more straightforward first- or second-order decay processes. Fluorescence lifetimes should have been observable and quantifiable, but have proven to be much more complex than we originally anticipated.

The baseline successes demonstrated by this work confirm the potential of SAMMS materials to provide a highly selective and sensitive detector for a variety of materials. Using Figure 1 as a benchmark, we have just barely finished with the characterization of Ac-Phos SAMMS loaded with europium (Figure 1b) and have not comfortably demonstrated the ability of trimethoxybenzene SAMMS material to bind an analyte of interest (Figure 1c). We anticipate having further successes either using these functional groups or others that are becoming available. This area of study promises to provide species-specific selectivity at low levels of detection. Subsequent work with 1,2,3-trimethoxybenzene will better quantify the interaction of functionalized SAMMS with aromatic hydrocarbons, with efforts focused on examining the effect of these compounds on fluorescence lifetimes. Work using the Ac-Phos SAMMS material is ready to progress to the next step, which involves examining the ability of the analyte to bind to the europium-loaded SAMMS and determining the effect of the bound analyte on the europium emission spectrum. Much work remains to be accomplished in this highly promising area of research.

Enzymatic Control of Humification

JE Amonette,[(a)] J Kim,[(a)] and CK Russell[(a)]
(a) Pacific Northwest National Laboratory, Richland, Washington

One of the approaches to minimizing the possible effects of climate change stemming from the recent and significant increases in atmospheric CO_2 levels involves fixing or storing carbon as biomass in terrestrial ecosystems. Of the possible terrestrial reservoirs for carbon storage, one of the most promising is organic matter in soil. Currently, this soil organic matter, called humus, contains about twice as much carbon as is present in the atmosphere. Our research has focused on understanding the fundamental process by which humus is created (i.e., humification) and extending this knowledge to enhance the rate of humification.

The rate-limiting step in the humification process appears to be the oxidation of polyphenols to quinones. These quinones then react with peptides and amino acids to form large melanin-like polymers that resist further degradation by microorganisms. We have observed a significant synergetic effect when a biological catalyst, such as a polyphenol oxidase (tyrosinase), and an inorganic catalyst, such as a mineral phase (e.g., mesoporous silica, manganese oxide, alkaline fly ash), are both present (Amonette et al. 2000, 2003a, 2003b).

In our experiments with alkaline fly ashes, the primary enhancing effect could be physical because of the presence of broken silica cenospheres, directly oxidative because of the presence of metal oxides, or indirectly oxidative because of the increase in pH. Our experiments, which were conducted using 10 wt% suspensions of the ash (i.e., 500 times more co-catalyst than with the metal oxides), showed humification enhancement factors of 2.4 ± 0.1 and 11 ± 2.3 for the lignitic and sub-bituminous ashes, respectively. Characterization of these ashes showed little difference in their cenosphere or metal oxide contents. However, a large difference in their titrateable alkalinity (pH 6.5) was observed, with that of the sub-bituminous fly ash (13.4 mmol/g) being about 4.6 times larger than that of the lignitic fly ash (2.9 mmol/g), the same factor by which their humification enhancement factors differed. Moreover, for the 0.5-g quantities used in the humification experiments, the alkalinities of both fly ashes were substantially greater than the capacity of the phosphate buffer (ca. 0.5 mmol) resulting in substantial pH increases in these experiments as the fly ashes equilibrated with the humic monomer solution. These results led us to investigate the effect of pH alone on the humification reaction.

Humification experiments at pHs of 5, 6.5, 7.5, and 9 clearly showed a substantial effect of alkaline pH on humification (Figure 1a). Essentially no humification occurred at pH 5, whereas maximal humification occurred at pH 9. Humification occurred primarily during the first 72 to 96 hours, and thereafter, little change was observed. Measurement of the enzyme activity during the experiment showed that activity held steady for perhaps 48 to 60 hours and then dropped rapidly to zero by 96 hours (Figure 1b). The enzyme activity at pH 9, however, was consistently smaller than that for any other pH, even though the same trend over time was observed. In the absence of tyrosinase, negligible amounts of humification were observed in all but the pH 9 treatments (Figure 1c), where maximum humification was still only about 5% of that observed when tyrosinase was present.

These results confirm the sequential two-step nature of the humification process—that is, oxidation of phenolic groups followed by condensation of the resulting quinones with amino acids to form melanins. High pH enhances the process primarily through its effect on the condensation step. Thus, maximum humification rates were obtained at pH 9 even though the enzyme activities were relatively low, whereas no humification was observed at pH 5 when enzyme activities were higher than at pH 9 (Figure 1a and b). Tyrosinase is needed for the reaction to occur at a useful rate (Figure 1c), but the level of tyrosinase activity seems less important than high pH in determining the yield of humic polymers. The manner by which condensation is enhanced likely relates to the speciation of the reactants at high pH. Quinones are stabilized, and the pKa of aliphatic amine groups is near 10. It could be that the anionic form of the amino acids (i.e., a neutral amine group) is critical to the condensation step.

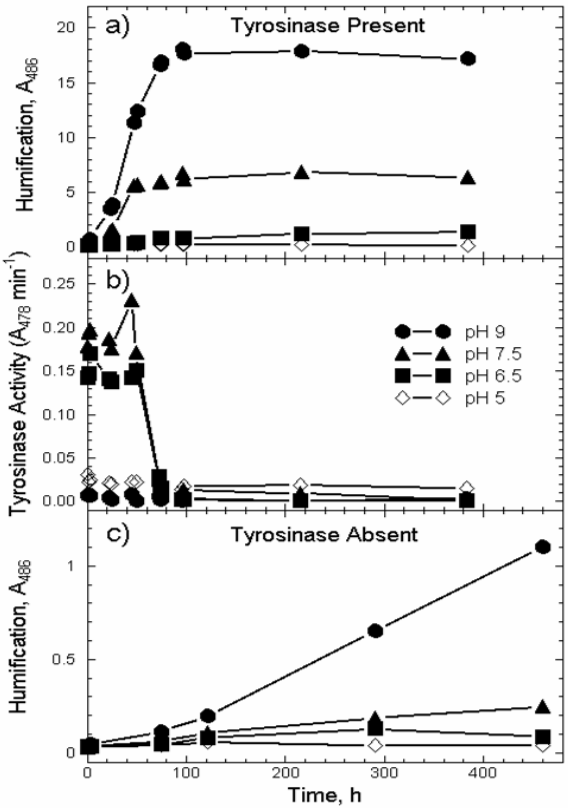

Figure 1. Effect of pH on rates of humification and on tyrosinase activity. (a) Humification with tyrosinase present. (b) Tyrosinase activity during the humification experiment. (c) Humification in the absence of tyrosinase.

References

Amonette JE, JA Capp, A Luttge, DR Baer, and RS Arvidson. 2000. "Geochemical Mechanisms in Terrestrial Carbon Sequestration." In *Annual Report 1999, Environmental Dynamics and Simulation*. PNNL-13206, pp. 3-23 to 3-27, Pacific Northwest National Laboratory, Richland, Washington.

Amonette JE, J Kim, CK Russell, AV Palumbo, and WL Daniels. 2003a. "Fly Ash Amendments Catalyze Soil Carbon Sequestration." In *Proceedings of the Second Annual Conference on Carbon Sequestration*, Alexandria, Virginia.

Amonette JE, J Kim, CK Russell, AV Palumbo, and WL Daniels. 2003b. "Enhancement of Soil Carbon Sequestration by Amendment with Fly Ash." In *Proceedings of the 2003 International Ash Utilization Symposium*, Lexington, Kentucky.

Effects of Sediment Iron Mineralogy on Microbially Mediated Changes in Divalent Metal Speciation: Importance of Ferrihydrite

DC Cooper,[(a)] AL Neal,[(b)] RK Kukkadapu,[(c)] DC Brewe,[(d)] A Coby,[(e)] and FW Picardal[(e)]

(a) Idaho National Engineering and Environmental Laboratory, Idaho Falls, Idaho
(b) University of Georgia, Aiken, South Carolina
(c) W.R. Wiley Environmental Molecular Sciences Laboratory, Richland, Washington
(d) Argonne National Laboratory, Argonne, Illinois
(e) Indiana University, Bloomington, Indiana

Dissimilatory metal-reducing bacteria (DMRB) can influence geochemical processes that subse-quently affect the speciation and mobility of metallic contaminants within natural environments. Most investigations into the effect of DMRB on sediment mineralogy use various synthetic Fe(III) oxides as the source, providing for well-controlled experiments. However, these oxides do not necessarily emulate the complex mineralogical composition of natural systems, nor do they account for the effect of complex sediment mineralogy on microbial activity and/or microbially induced geochemical processes. Our experiments with a pure DMRB culture (*Shewanella putrefaciens* 200) and a divalent metal [Zn(II)] indicate that, while complexity in sediment iron mineralogy may not strongly impact the degree of "microbial Fe(III) reducibility," this complexity does alter the geochemical effect of such microbial activity. These experiments also demonstrate that, regardless of sediment composition, the ferrihydrite [poorly crystalline Fe(III)-oxide] content is of central importance.

Changes in Zn(II) chemistry were quantified through a combination of chemical extractions and x-ray absorption spectroscopy analysis on reduced sediments and sterile controls. In a synthetic goethite and ferrihydrite mixture, Zn(II) was originally adsorbed to iron oxide surfaces via outer-sphere surface complexes. Upon reduction, the amount of acid-soluble Zn(II) reduced dramatically and Zn *k*-edge extended x-ray absorption fine-structure spectroscopy data demonstrated a slight increase in the degree of second order, Zn-O-Zn/Fe interactions. This shift was not observed in natural sediments containing predominantly quartz, hematite, and kaolinite/illite clays, even though the original Zn(II) binding was similar to that in the synthetic goethite/ferri-hydrite mixture. Here, microbial Fe(III) reduction resulted in the formation of an outer-sphere $ZnCl_2$ complex and did not affect the degree of Zn(II) acid solubility.

Mössbauer analyses were central to these experiments, and provided key evidence that the differences in the geochemical effect of microbial Fe(III) reduction were related to the ferrihydrite content of the Fe-oxide/sediment. Liquid nitrogen (77 K) Mössbauer data for synthetic goethite/ferrihydrite reveal a loss of the central doublet upon microbial reduction and subsequent re-oxidation, indicating preferential loss of ferrihydrite (Figure 1a and b). This Mössbauer data (taken at 77 K) for the natural sediment (Figure 1c and d) reveal a different response to microbial Fe(III) reduction. Here, a combination of Mössbauer spectroscopy and chemical extractions specific for poorly crystalline iron oxide minerals has indicated that the central doublet (Figure 1c) arises from sedimentary clay minerals and not from the ferrihydrite. The doublet is representative of structural Fe(II) in the illite clays, and the sextet arises from the contribution of iron oxide minerals identified by x-ray diffraction

to be hematite. In Figure 1d, spectra of the unreduced material and the sample that has been reduced and then re-oxidized are compared. Comparison of these data reveals that, unlike the synthetic goethite/ferrihydrite, microbial Fe(III) reduction did not permanently alter the iron speciation in this sediment. Also, because previous work has demonstrated that microbial reduction of structural Fe(III) in illite clay significantly alters the Fe(II)/Fe(III) ratio of the reduced and re-oxidized clay as compared to the unreduced clay, it can be concluded that Fe(III) in iron oxides was microbially reduced. Room temperature Mössbauer data indicated that 1) the percent of total peak area attributable to Fe-oxide agreed with results from chemical extractions, and 2) apparent Mössbauer parameters did not reflect the presence of siderite or green rust (data not shown).

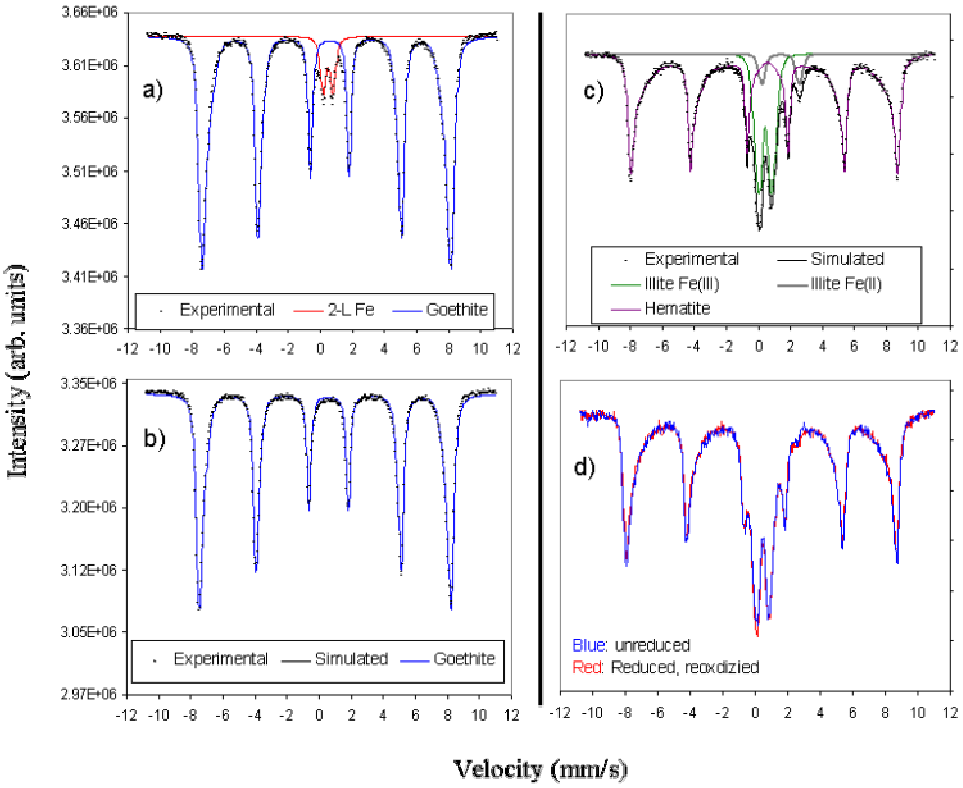

Figure 1. Liquid nitrogen (77 K) Mössbauer data for synthetic goethite/ferrihydrite. (a) Unreduced synthetic goethite/ferrihydrite mixture. (b) Reduced and re-oxidized goethite/ferrihyrite mixture. (c) Unreduced natural sediment. (d) Reduced and re-oxidized sediment.

The preferential loss of ferrihydrite in the synthetic goethite/ferrihydrite stands in contrast to the retention of more crystalline iron oxides (goethite, hematite) in both sediments, and indicates that reactions involving ferrihydrite are responsible for the changes in Zn(II) acid solubility observed for the synthetic goethite/ferrihydrite. When this evidence is considered in light of earlier studies indicating that the addition of Fe(II) to ferrihydrite can catalyze transformation of ferrihydrite to goethite, it becomes apparent that ferrihydrite may stimulate a sequence of geochemical reactions that would not occur in its absence. Experiments to specifically test the effect of ferrihydrite addition to iron-bearing sediments are currently under way.

Biotransformation of Silica-Ferrihydrite by a Dissimilatory Fe(III)-Reducing Bacterium (DIRB): Formation of Carbonate Green Rust in the Presence of Phosphate

RK Kukkadapu,[(a)] JM Zachara,[(b)] JK Fredrickson,[(b)] and DW Kennedy[(b)]
(a) W.R. Wiley Environmental Molecular Sciences Laboratory, Richland, Washington
(b) Pacific Northwest National Laboratory, Richland, Washington

Dissimilatory Fe(III)-reducing bacterium catalyze the reduction of Fe(III) to Fe(II) in anoxic soils, sediments, and groundwater. A variety of biomineralization products result from the interaction of DIRB with ferrihydrite, including green rust (GR) $\{[Fe^{II}_{(6-x)}Fe^{III}_{x}(OH)_{12}]^{x+}(A^{n-})_{x/n}.yH_2O$; where $A = CO_3^{2-}\}$, and magnetite (Fe_3O_4), under specific conditions (Zachara et al. 2002). Both magnetite and GR are mixed valence Fe(II)/Fe(III) compounds. GRs are potential contaminant reductants, anion exchangers, and metal cation sorbents.

Naturally occurring ferrihydrite contains significant amounts of SiO_4^{4-} (Si), and PO_4^{3-}(P). Sorbed Si and P have strong affinity for ferrihydrite. The objective of this study was to investigate the combined effects of Si and P on bioreducibility and biomineralization of ferrihydrites under anoxic conditions by *Shewanella putrefaciens*, which is a DIRB. The influence of these anions on ferrihydrite biotransformation was explored by varying the Si content of the ferrihydrite coprecipiates and the P content of the medium.

Ferrihydrite was rapidly reduced regardless of Si and P content. In the range studied (Si/[Si+Fe] mole fraction of 0.01 and 0.05), Si concentration had no effect on the reduction rate or the mineralization products. The P-concentration (P/[P+Fe] mole fraction of 0.01 to 0.2 or 1 to 20 mM P for 50 mM Fe), however, had a profound effect on the extent of ferrihydrite reduction and bio-transformations. A magnetite-like compound was formed in the absence of P, whereas GR(CO_3^{2-}) and vivianite [$Fe_3(PO_4)_2$•$8H_2O$] were formed when P was present (in both Si ferrihydrites). GR(CO_3^{2-}) dominated as a mineral product in samples with <4 mM P, while vivianite dominated when the mole fracton of P was higher.

In addition to the ferrihydrite, GR and vivianite evident by x-ray diffraction (XRD), other Fe species were tentatively identified in the bioreduced mineral residues: 1) GR-like phase (GR*), 2) sorbed Fe(II), and 3) a mixed Fe(II) and Fe(III) superparamagnetic (*spm*) phase. These transitory Fe(II)-containing species were identified by their Mössbauer response (temperature) and apparent lability towards oxygen during the XRD analyses. GR* exhibited Mössbauer parameters similar to GR at room temperature and at 77 K, but unlike GR, GR* rapidly oxidized to ferrihydrite during XRD analysis. Sorbed Fe(II) differed from GR and GR* in that it was "invisible" in the room-temperature Mössbauer spectra and appeared as a doublet in the 77-K spectra. Sorbed Fe(II) may exist in an adsorbed state or as poorly crystalline precipitate. Sorbed Fe(II) was also rapidly oxidized when contacted with air. The *spm* phase exists in our Mössbauer spectra as doublet at room temperature and as a collapsed sextet at 77 K.

GR(CO_3^{2-}) appeared to form by solid-state transformation of ferrihydrite. Media P and Si concentration dictated the mechanism of transformation. The transformation of GR* and *spm* Fe to GR in the 0.01-Si-ferrihydrite with 1 mM P with time was clearly evident from Figures 1a and 1b. During this time period (approximately 15 months) there was no additional Fe(II) production. The GR formation mechanism was different at higher anion "loadings." In the media containing higher Si and/or P, sorbed Fe(II), GR* and residual ferrihydrite (RF) transformed to GR with time (with no additional Fe(II) production). This was clearly evident from the spectra of 0.01-Si-ferrihydrite that was incubated in 4 mM P (Figures 1c and 1d).

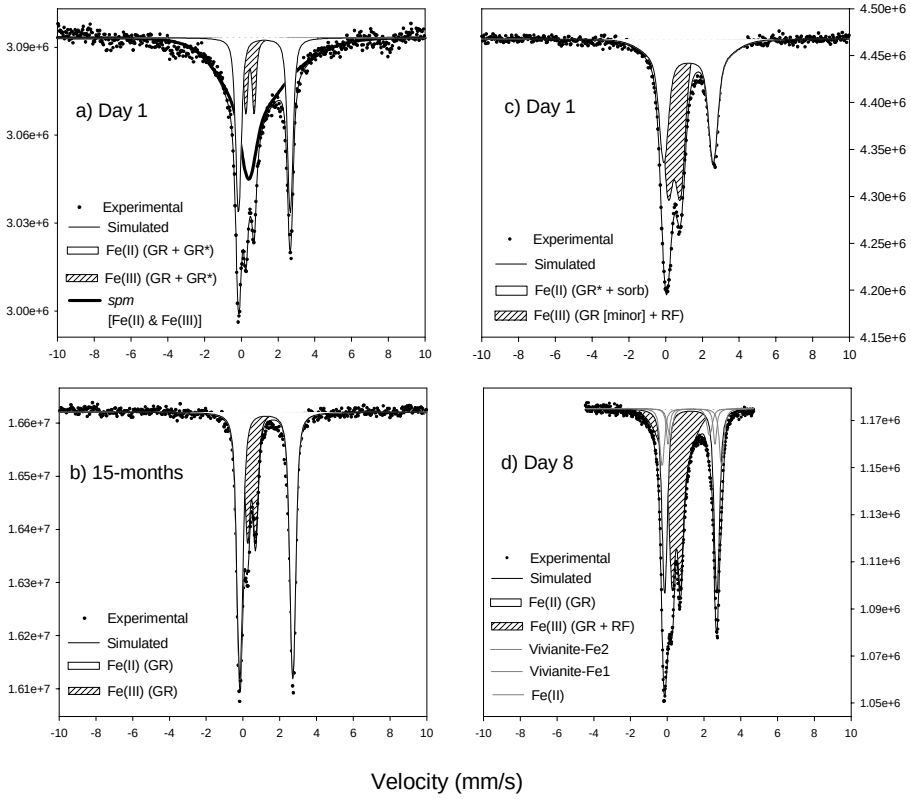

Figure 1. 77 K Mössbauer spectra of 0.01-Si-ferrihydrite. (a)-(b) 1 mM P after a day and 15 months, respectively. (c)-(d) 4 mM P after 1 and 8 days, respectively.

The study clearly showed that P played a significant role on GR(CO_3^{2-}) formation, albeit indirect, particularly in the systems where its content is low (<4 mM P). The non-effect of Si on overall activity, formation of magnetite in the absence of P, and the formation of GR(CO_3^{2-}), but not GR(PO_4^{3-}), in the presence of P have several environmental implications because both Si and P are generally found associated with ferrihydrites in natural environments.

Reference

Zachara JM, RK Kukkadapu, JK Fredrickson, YA Gorby, and SC Smith. 2002. "Biomineralization of Poorly Crystalline Fe(III) Oxides by Dissimilatory Metal-Reducing Bacteria (DMRB)." *Geomicrobiology Journal* (19):179-207.

Imaging and Analysis of Nanostructures and Biominerals Associated with Bacterial Envelopes

A Dohnalkova[(a)] and JK Fredrickson[(a)]
(a) Pacific Northwest National Laboratory, Richland, Washington

Transmission electron microscopy (TEM) represents a powerful imaging technique for examining the bacterial interior, boundary layers including plasma membranes, cell walls, and the outer membrane structures such as peptidoglycans and extracellular polysaccharides, and proteins (Figure 1 [left]).

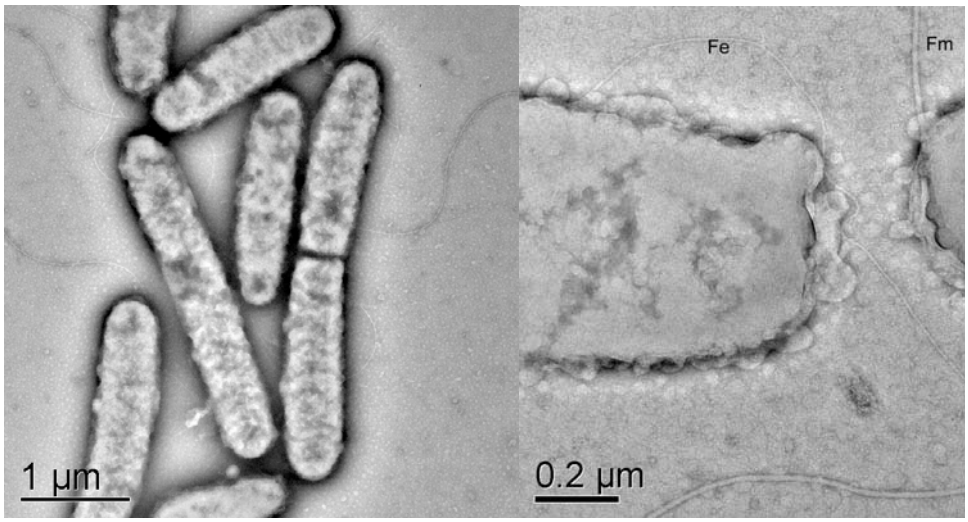

Figure 1. Left: TEM image of a Gsp mutant of *S. oneidensis* MR-1 cells. Right: Bacterial surface features and appendages such as flagella (fm) and fimbriae (Fe) are visualized by negative staining with ammonium molybdenate. The diameter of flagella is approximately 12 nm.

Observations of ultrathin sections prepared traditionally by microtomy of plastic-embedded, chemically fixed specimens are still considered a standard procedure for examining cell structures. Several new techniques, however, are replacing the classical chemical methods of fixation by cryoprocessing, bringing impressive advances in preservation of bacterial morphology. During the past few years, TEM has achieved tremendous improvement in spatial resolution, to some extent because of the rapid advance in methods of molecular biology demanding visualization of newly identified macromolecular constituents. Remarkable development in methods using immuno-cytochemistry and three-dimensional imaging techniques also advanced TEM as a relevant technique.

This paper presents an overview of the state-of-the-art imaging methods we used to characterize the process of metal reduction by the dissimilatory metal-reducing bacterium *Shewanella oneidensis* strain MR-1. Our research has focused recently on membrane protein translocation and secretion, particularly on analysis of type IV-like pili and other proteins associated with the type-II secretion system. Recent evidence suggests that bundled pilins may play a key role in the export of newly formed biominerals, such as uraninite (UO_2), from sites of reduction in the periplasm through the outer membrane.

Visualization of these proteins and their assemblages is a significant challenge, given the nanoscale dimension and electron transparency of these structures. Contrast enhancement by negative stains on whole mount preparations has been used as a method of choice for their visualization (Figure 1 [right]). Immuno-gold labeling with nanogold particles conjugated to the secondary antibody serves as a specific means for labeling proteins with these assemblies.

We have addressed other electron microscopy approaches previously developed for the eukaryotic cells and customized for prokaryotes. These approaches include freeze fracturing for high-resolution morphology of membrane structures, immunogold labeling of proteins with emphasis on a choice of a suitable nanogold tag, mapping of areas of electric charge by charged nanogold, negative contrasting of filamentous appendages like flagella and fimbriae, electron diffraction and atomic-level TEM used for identification of membrane-associated biominerals, and the innovative three-dimensional reconstruction of a bacterial cell by TEM electron tomography. These analyses are lending new insights into the mechanism by which bacteria interact with metals and control dissolution and precipitation reactions.

Sorption Versus Biomineralization of Pb(II) within *Burkholderia cepacia* Biofilms

AS Templeton,[(a)] TP Trainor, [(a,b)] AM Spormann, [(a)] M Newville,[(c)] SR Sutton,[(c)] A Dohnalkova,[(d)] Y Gorby, [(d)] and GE Brown[(d)]

(a) Stanford University, Stanford, California
(b) University of Chicago, Chicago, Illinois
(c) Argonne National Laboratory, Argonne, Illinois
(d) Pacific Northwest National Laboratory, Richland, Washington

X-ray spectroscopy measurements have been combined with macroscopic uptake data and transmission electron microscopy (TEM) results to show that Pb(II) uptake by *Burkholderia cepacia* is caused by simultaneous sorption and biomineralization processes. X-ray microprobe mapping of *B. cepacia* biofilms formed on R-Al_2O_3 surfaces shows that Pb(II) is distributed heterogeneously throughout the biofilms because of the formation of Pb "hot spots." Data from extended x-ray absorption fine-structure (EXAFS) analysis and TEM observations show that the enhanced Pb accumulation is caused by the formation of nanoscale crystals of pyromorphite [$Pb_5(PO_4)_3(OH)$] adjacent to the outer membrane of a fraction of the total population of *B. cepacia* cells (Figure 1). In contrast, *B. cepacia* cell suspensions or biofilms that were heat-killed or pretreated with x-rays do not form pyromorphite, which suggests that metabolic activity is required. Precipitation of pyromorphite occurs over several orders of magnitude in [H+] and [Pb] and accounts for approximately 90% of the total Pb uptake below pH 4.5 but only 45 to 60% at near-neutral pH because of the formation of additional Pb(II) adsorption complexes. Structural fits of Pb LIII EXAFS data collected for heat-treated cells at near-neutral pH suggest that Pb(II) forms inner-sphere adsorption complexes with carboxyl functional groups in the biofilms.

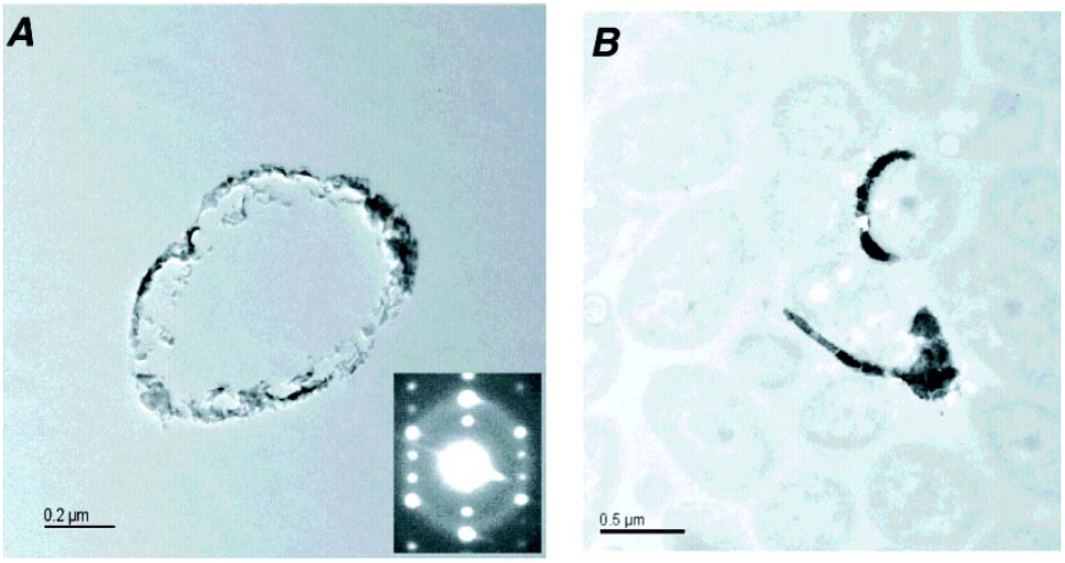

Figure 1. Transmission electron micrographs of *B. cepacia* incubated with 10-4.3 M $Pb(NO_3)_2$, pH 6. (A) Electron-dense Pb precipitates are associated with the cell membranes. Inset: selected-area diffraction pattern of the material reveals its crystalline nature. (B) Thin section with the material was post-stained with uranyl acetate to visualize the cells.

The pyromorphite formation during uptake of Pb(II) by *B. cepacia* is due to both adsorption and biomineralization processes according the EXAFS spectra. Independent confirmation that pyromorphite is present at the outer-membrane of *B. cepacia* was obtained from the TEM imaging coupled with selected-area diffraction data. The localized hot spots of Pb accumulation are likely regions where a few cells are significantly biomineralized because of the formation of lead phosphate [$Pb_3(PO_4)_2$] at the surface of individual bacterial cells. These interpretations are supported by the grazing-incidence EXAFS data, which indicate that both sorbed Pb(II) and pyromorphite are associated with *B. cepacia.* The formation of pyromorphite is biologically controlled and discretely localized, requiring a source of phosphate from *B. cepacia* for the precipitation of a lead phosphate phase. Live/dead staining of *B. cepacia* suspensions incubated with high [Pb] show that greater than 90% of the cells are still viable after 24 hours.

The mechanism of $Pb_3(PO_4)_2$ formation by *B. cepacia* is unknown. Passive surface complexation reactions outside bacterial cells and in the exopolysaccharide can lead to the accumulation of metal-bearing minerals (Templeton et al. 2003). For *B. cepacia*, we have observed $Pb_3(PO_4)_2$ formation at the bacterial surface but have not found any evidence for Pb accumulation within the cytoplasm, which is consistent with observations for other Gram-negative bacteria. Both adsorption and precipitation occur rapidly, on the order of minutes. The data presented here are from 24-hour incubations of *B. cepacia* with Pb-bearing solutions. However, additional experiments where *B. cepacia* was reacted with $10^{-4.3}$ M Pb at pH 6 for 5, 15, and 30 minutes show that 90% of the total uptake has occurred within 5 minutes, resulting in measurable pyromorphite formation (32% total uptake). By 30 minutes, steady-state [Pb] has been reached, and the fraction of Pb(II) sorption complexes relative to pyromorphite falls within the same range of values as reported for the 24-hour experiments (65% pyromorphite). Therefore, given the immediate metabolic response, the enzymatic activity required for $Pb_3(PO_4)_2$ precipitation is likely constitutive, although it may also be inducible to higher levels under appropriate conditions.

The biomineralization of nanoscale hydroxypyromorphite significantly reduces the activity of Pb(II) in the biofilms because of the formation of such a sparingly soluble phase. Given the common occurrence of pyromorphites in Pb-contaminated soils and the widespread distribution of Pb-resistant soil isolates, it is worthwhile to consider the conditions under which bacteria may act as primary agents in the formation of recalcitrant Pb-P phases in soils with high Pb activity.

Reference

Templeton AS, TP Trainor, AM Spormann, M Newville, SR Sutton, A Dohnalkova, Y Gorby, and GE Brown. 2003. "Sorption Versus Biomineralization of Pb(II) within *Burkholderia cepacia* Biofilms." *Environmental Science & Technology* 37:300-307.

The Statistical Identification of Bacteria from FTIR Spectra

NS Foster,[(a)] TJ Johnson,[(b)] NB Valentine,[(b)] SE Thompson,[(b)] and JE Amonette[(b)]
(a) W.R. Wiley Environmental Molecular Sciences Laboratory, Richland, Washington
(b) Pacific Northwest National Laboratory, Richland, Washington

Rapid bacterial detection and identification is important in health care facilities, the food industry, and in signaling the possible (malicious) release of biological agents. Various methods for bacterial identification have been employed including culturing, antigen/antibody methods, polymerase chain reaction (PCR) analysis, and mass spectrometry. In many applications, time is often critical in the identification of certain pathogens, and both the culturing and PCR techniques are time consuming. While many of the mass spectrometry methods offer good sensitivity and high specificity, the nature of the experiments (involving preparatory methods and several pumps) does not lend itself to the development of either rapid methods or man-portable devices.

This report summarizes a combined mid-infrared spectroscopic/statistical modeling approach for discriminating and identifying, at the strain level, both sporulated and vegetative bacteria using two different Fourier transform infrared (FTIR) spectroscopy techniques (Foster et al. 2004a, 2004b; Thompson et al. 2003): photoacoustic (PA-FTIR) and transmissive (trans-FTIR) (Figure 1).

For each technique, a reference spectral library was compiled by collecting two to four individual spectra for each of two or three batches of each grown or sporulated bacterial strain. A total of 138 spectra (40 sporulated, 98 vegetative) were collected for the trans-FTIR library, and a total of 40 spectra (sporulated only) were collected for the PA-FTIR library. Principal component analysis and Mahalanobis distances were used to create classification and regression trees (Figure 2) to classify bacterial stain data. To assess the stability of the model, cross-validation was used in all steps of the model. In cross-validation, one sample is removed from the dataset, the procedure is performed, and the result for the removed sample is recorded. The analysis and results for each library were encouraging. The model was able to classify not only the physical state (spore/vegetative) but to also identify a sample down to the individual strain level.

For external validation, spectra for "blind" samples were collected for each technique and analyzed using the statistical model. Blind samples generally included reference and other bacteria, nonbio-logical materials, and mixtures of both nonbiological and bacterial samples.

For external validation using blind samples, the success was more limited. The non-bacterial samples were quickly discriminated against, and bacterial "blinds" that were members of the library were identified as such, but certain blind bacterial samples that were not members of the library were identified as being in the library (a false positive result). However, in most cases the false positives were identified correctly at the species level or identified as a species that was very similar in nature.

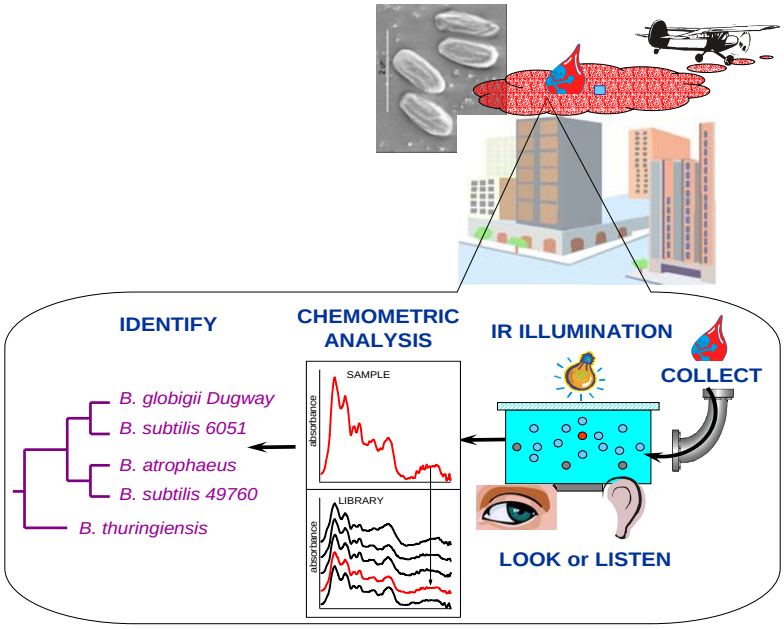

Figure 1. The recently heightened awareness of the threat posed by biological agents has stimulated much research to develop both rapid and accurate methods for the detection of pathogenic bacteria. This graphic depicts a scenario involving an airplane releasing bacterial spores (inset: scanning electron microscope image of *Bacillus subtilis* ATCC 49760 spores). The graphic then outlines a method for collection followed by spectroscopic and chemometric analysis. The research in this highlight describes a spectroscopic and statistical feasibility study for the identification (at the strain level) of bacteria (spores or vegetative). In PA-FTIR spectroscopy, the infrared (IR) light is focused onto the sample (ILLUMINATE), which ultimately generates an acoustic wave in the surrounding gas with the sound detected by a microphone (LISTEN). In trans-FTIR spectroscopy, the IR light is focused onto the sample (ILLUMINATE) and the amount of light absorbed (LOOK) is calculated. Several *Bacillus* bacterial strains were used to construct a reference spectral library and to parameterize a statistical model for the systematic identification of bacterial spores. The feasibility study used common chemometric tools for the analysis of the library components and interferants, including the analysis of "blind" samples.

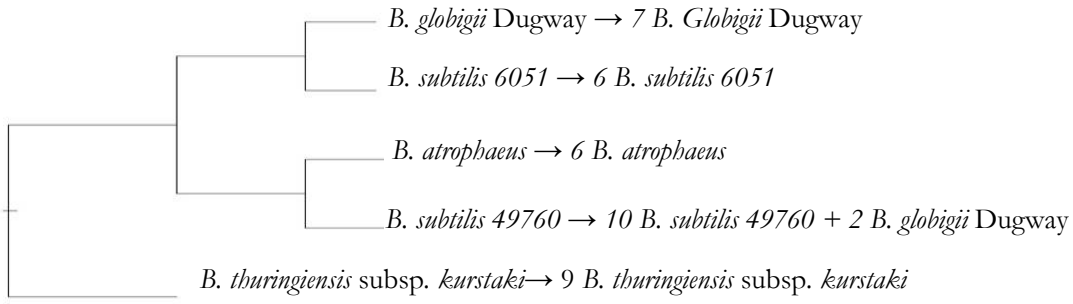

Figure 2. Example of a classification and regression tree (CART) tree. PA-FTIR reference library data for bacterial spores.

We have demonstrated for the first time, a nondestructive, optical spectroscopic method that requires little or none of the sample preparation required for PA-FTIR spectroscopy to identify and speciate bacterial spores. Our results, while promising, are only the first step in the development of this method for routine detection. Future work will focus on continued construction of a larger reference library containing spectra for additional species and strains, and further investigation into how different methods of sample preparation (e.g., different growing conditions) affects results would also be clearly worthwhile. Both the spectroscopic technique and the chemometric methods are also being investigated to increase the identification rate.

The trans-FTIR and PA-FTIR methods show great promise for use in rapidly detecting bacteria and, in particular, spores. With an appropriate particle collector, air samples could be monitored and analysis completed within approximately 5 minutes or less. While semi-portable FTIR units exist, a more simplified approach would be to design a fixed-wavelength sensor that relies on only a few specific frequencies. We are in the process of applying a genetic algorithm to this same dataset to determine the minimum number of infrared wavelengths required to speciate spores (Foster et al. 2004a).

References

Foster NS, NB Valentine, SE Thompson, TJ Johnson, JE Amonette, and A Heredia-Langner. 2004a. "FTIR Transmission and Photoacoustic Spectroscopy for the Statistical Identification of Bacteria." *SPIE Photonics East Conference Proceedings: Chemical and Biological Point Sensors for Homeland Defense Symposium*, eds. AF Sedlacek III, SD Christesen, R Colton, and T Vo-Dinh, vol. 5269 pp. 172-182. Providence, Rhode Island.

Foster NS, SE Thompson, NB Valentine, JE Amonette, and TJ Johnson. 2004b. "Identification of Sporulated and Vegetative Bacteria Using Statistical Analysis of Fourier Transform Mid-Infrared Transmission Data." *Applied Spectroscopy* 58:203-211.

Thompson SE, NS Foster, TJ Johnson, NB Valentine, and JE Amonette. 2003. "Identification of Bacterial Spores using Statistical Analysis of Fourier Transform Infrared Photoacoustic Spectroscopy Data." *Applied Spectroscopy* 57(8):893-899.

Quantification of Organics in Supercritical Fluid Aging Experiments Using FTIR Spectroscopy

CJ Thompson,[(a)] RG Riley,[(a)] JE Amonette,[(a)] and PL Gassman[(b)]

(a) Pacific Northwest National Laboratory, Richland, Washington

(b) W.R. Wiley Environmental Molecular Sciences Laboratory, Richland, Washington

Aging is a term used to describe the slow accumulation of hydrophobic organic compounds in the mineral pores and natural organic matter of soils and sediments over extended periods of time (e.g., decades). Contaminants in aged materials exhibit decreased bioavailability and slow release to the environment. Therefore, aging may have a significant influence on the applicability and effectiveness of remediation strategies (e.g., bioremediation and natural attenuation) and the accuracy of numerical transport models. Efforts to understand and quantify the effects of aging have been hindered by an inability to accurately simulate the aging process on a short timescale. Previous research in our laboratory has demonstrated that circulating supercritical CO_2 (SC-CO_2) can be used to rapidly prepare artificially aged materials for studying slow-release behavior (Riley et al. 2001). One of the key features of this methodology has been the ability to monitor the progress of the simulated aging process in real time using an in-line, ultraviolet (UV) light detector. Many contaminants of interest, however, do not absorb in the UV range and cannot be monitored using our previous approach.

In this investigation, Fourier transform infrared (FTIR) spectroscopy was evaluated as an alternate detector for artificial aging experiments. Compared to single-wavelength UV detection, FTIR spectroscopy has the potential advantages of 1) providing nearly universal detection of organics and 2) the ability to monitor multiple contaminants simultaneously.

We interfaced a FTIR spectrometer to a supercritical fluid loading apparatus using a high-pressure flow cell with a 1-mm path length. Infrared spectra of SC-CO_2 and xenon were obtained at several temperature and pressure conditions. Xenon was evaluated because we anticipated that the strong absorbance of CO_2 would interfere with the measurement of certain compounds of interest. We next measured the infrared spectra of several selected halocarbons in supercritical xenon and CO_2 (Figure 1). The two sets of spectra are very similar, although the band intensities are slightly reduced in SC-CO_2, and some of the bands associated with C-X stretches are partially or fully masked by CO_2 absorbance in the SC-CO_2 spectra. Nonetheless, the unique spectral fingerprints of the compounds investigated

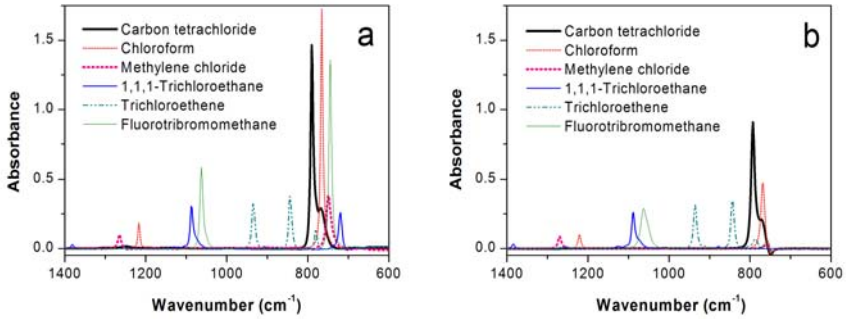

Figure 1. FTIR absorbance spectra of selected halocarbons in (a) supercritical Xe and (b) SC-CO_2. Temperature and pressure were held constant at 35°C and 200 atm.

demonstrate that multiple compounds (e.g., a contaminant and its degradation products) can be monitored simultaneously using FTIR spectroscopy. Moreover, the spectra indicate that the use of supercritical xenon as a solvent is not necessary for monitoring the compounds in this study. This is advantageous because CO_2 is cheaper and more widely available than xenon.

Varying amounts of carbon tetrachloride (CCl_4), a volatile contaminant of concern at the Hanford Site, were mixed with SC-CO_2 (200 atm, 35°C), and the spectra of the resulting solutions were measured (Figure 2a). The apparent wave number shift in the spectra with increasing concentration was determined to be a saturation artifact associated with the infrared detector. Single-wavelength calibration on the shoulder of the primary absorbance band (793 cm^{-1}) produced excellent results over a broad concentration range (Figure 2b). Based on the variability of the SC-CO_2 baseline, we determined the detection limit to be approximately 2 mM. If desired, lower concentrations could be measured using a wavelength near the center of the absorbance band.

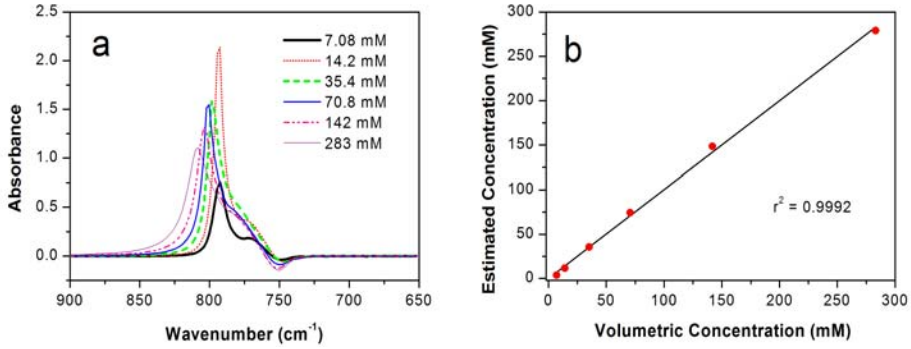

Figure 2. Quantification of CCl_4 in SC-CO_2: (a) FTIR spectra of CCl_4 solutions (b) single-wavelength calibration results (814 cm^{-1}).

Infrared detection was used to monitor the artificial aging of two soils (Hanford and Iron River) with CCl_4. In each experiment, an SC-CO_2 solution containing CCl_4 was circulated for 4 hours through a soil column. Periodically, infrared spectra of the supercritical fluid were measured, and decreases in concentration were attributed to incorporation of the CCl_4 into the soil. Estimates of soil concentrations from the infrared spectra were approximately 2 to 4 times higher than the concentrations determined from off-line gas chromatograph (GC) analyses of soil extracts. We believe the discrepancies were caused by partial removal of CCl_4 from the soil during depressurization of the loading apparatus and sample instability (i.e., volatilization of the CCl_4) prior to the GC analysis. Despite potential changes in samples during depressurization, this research has demonstrated that FTIR spectroscopy is a powerful tool for monitoring the progress of artificial aging experiments. Future work may enable us to closely relate FTIR-based concentration estimates to final loaded concentrations.

References

Riley RG, CJ Thompson, MH Huesemann, Z Wang, B Peyton, T Fortman, MJ Truex, and KE Parker. 2001. "Artificial Aging of Phenanthrene in Porous Silicas Using Supercritical Carbon Dioxide." *Environmental Science & Technology* 35(18):3707-3712.

Investigation of Near-Infrared Optical Parameters in Fish Tissue by Photon Time-of-Flight Analysis

JL Wutzke,[(a)] CA Fahlstrom,[(a)] AG Cavinato,[(a)] Z Wang,[(b)] AG Joly,[(b)] M Lin,[(c)] and BA Rasco[(c)]

(a) Eastern Oregon University, La Grande, Oregon
(b) Pacific Northwest National Laboratory, Richland, Washington
(c) Washington State University, Pullman, Washington

Near-infrared (NIR) spectroscopy has shown great promise for the non-destructive analysis of complex samples in diagnostic medicine and in the agricultural industries for routine analysis of cereal grains and meat composition.

When light interacts with tissues, different processes can occur. Some of the light can be reflected off the surface, while the rest enters the tissue. Inside the tissue, the light can be absorbed or scattered. Both phenomena are highly dependent on the wavelength of incident light. The NIR region is characterized by low tissue absorbance but relatively high tissue scattering. Particles will scatter electromagnetic radiation if they have a refractive index that differs from that of the supporting material. Scattering in tissue may be due to refractive index changes at cell walls and within cells and organelles. Tissue scattering has the general form of λ^{x} where λ is the wavelength and x is dependent on the tissue type. Scattering phenomena are particularly complex for non-homogeneous tissues and introduce additional challenges with quantitative short wavelength (SW)-NIR measurements.

One of the most important parameters in quantitative analysis is the path length of the light that travels between input fiber and output fiber. Path length determination is particularly challenging for measurements conducted in diffuse reflectance due to multiple scattering phenomena. In this study, we used time-correlated spectroscopy to determine the path length of SW-NIR light in fish tissue.

We determined the path length directly by time-correlated photon counting using a Hamamatsu 3680 high-speed streak camera that was illuminated with a Clark-MXR NJA-5 Ti:Sapphire laser (76 MHz), which in turn was pumped with a Spectra-Physics Millennia Nd:YAG laser. In this approach, a short pulse of light is launched into a medium of thickness x. If the medium is non-scattering, the light travels with a velocity $v = c/n$ where n is the index of refraction of the medium and c is the speed of light in vacuum. The pulse will exit at a time $t = x/v$. In a scattering medium, most of the light will be scattered and will exit at a time later than $t = x/v$. Photons that take a direct path will arrive at the detector earlier; those taking a longer path will arrive later. This transit time difference is used to generate a temporal point spread function (TPSF) from which the average transit time t of photons through the medium can be calculated. The transit time can then be converted into distance traveled through the medium, $Distance = c\,t/n$. Minced cod samples of varying lipid and salt concentration were produced (N=46). Lipid concentration in the sample varied in the range of 0 to 18% by weight. Canola oil was used as the source of lipid. Salt samples were produced in the range of 0 to 10% salt by weight. Whole and smoked salmon samples (N=160) were used for measurements. Mean photon path length for each sample was calculated by multiplying the mean time of flight by the speed of light in tissue

(0.214mm/ps). The mean time of flight (τ) was calculated as $\tau = \int t\, I\, dt$ and $\int I\, dt$, where I is the light intensity at each time t. This method differs from previous methods but is a more direct result of diffusion equation calculations.

Figure 1 shows the integrated TPSFs recorded on Chinook salmon tissue after the skin and scales were removed. It can be seen that considerable temporal dispersion occurs due to multiple scattering of the light in the fish tissue. As expected, increasing times of flight and decreasing intensity were recorded for increasing distance between the source fiber and the pick-up fiber.

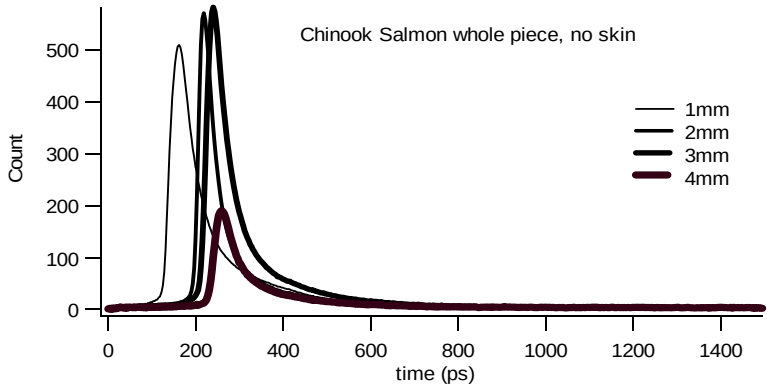

Figure 1. Time of flight profiles for Chinook salmon.

For the minced cod samples, the path lengths do not vary significantly as lipid concentration of the samples increases from 0 to 20%. Similar results were obtained when measuring the path lengths for cod samples of varying salt concentrations. These results reveal that the light path length in a highly scattering tissue sample is not affected significantly by either varying lipid concentrations or salt concentrations. However, the absolute path length value for each source/pick-up fiber configuration differs for samples containing only lipid versus samples containing only salt. In general, for the same source/pick-up fiber distance, samples containing only varying amounts of lipid show path lengths 1.5 times larger than samples with only varying amounts of salt. Additional time-of-flight measurements performed on intact and smoked salmon samples of varying lipid and salt concentrations show that there are no major differences in the interaction of light with tissues of variable composition. The measured path length varies between 50 and 60 mm with no significant or obvious trend.

These results suggest that the presence of lipids in fish tissue samples may increase multiple scattering effects, thus yielding longer path lengths than in the absence of lipid. This study shows that, on average, the light path length in samples containing only lipid is 1.5 times larger than in samples containing only salt. However, no significant changes occur when varying the concentration of each analyte. It is possible that the sensitivity of the streak camera maybe not be suitable for detecting such subtle changes. It was our original hypothesis that path length would be affected by changes in the concentrations of the constituents, thus introducing non-linearities when developing calibration models for determining fish and fish products constituents such as lipid, moisture, and salt.

Cryogenic Laser-Induced Fluorescence Characterization of U(VI) in Hanford Vadose Zone Pore Waters

Z Wang,[a] JM Zachara,[a] W Yantasee,[a] PL Gassman,[b] CX Liu,[a] and AG Joly[a]
(a) Pacific Northwest National Laboratory, Richland, Washington
(b) W.R. Wiley Environmental Molecular Sciences Laboratory, Richland, Washington

The presence of U(VI) complexes with carbonate are important factors in the risk assessment and formulation of decontamination strategies for the remediation of uranium-contaminated soils and sediments. The concentration of U(VI) is typically on the order of 10^{-7} M or lower in groundwater and 10^{-5} M in mining waters, which are below the detection limit of many spectroscopic techniques such as infrared (IR), Fourier transform infrared (FTIR), Raman, x-ray diffraction (XRD), and extended x-ray absorption fine-structure spectroscopy (EXAFS). Thus far, the most sensitive technique for the analysis of dilute U(VI) solutions has been the fluorescence-based techniques. The intensity, bandwidth, and spacing of the vibronic bands of uranyl fluorescence spectra and its fluorescence lifetime are highly sensitive to the bonding, symmetry, and local chemical environment of uranyl ion, and thus provide useful tools for the study of uranyl speciation.

We have recently demonstrated that, at near-liquid helium temperature (LHeT), the intensity and resolution of the fluorescence spectra of uranyl-silicate minerals could be significantly improved, making it possible to identify the speciation of uranyl in vadose zone sediments at the Hanford Site. We have successfully used this technique to characterize a series of aqueous uranyl-carbonate, one-phosphate complexes, and two sediment pore-water samples from the Hanford-site vadose zone. At LHeT, all the complexes displayed strong, well-resolved fluorescence emission spectra. A comparison of the spectra of the Hanford vadose-zone pore waters to those of the standard uranyl-carbonate/phosphate complexes confirmed that the Hanford-site pore waters contain mainly 1:3 uranyl carbonate complexes.

A set of standard U(VI)-carbonate solutions were designed and synthesized to assist in the identification of aqueous U(VI) species in the sedimentary pore-water samples. Specific solution conditions (pH, CO_2 partial pressure, and concentrations of reactants) were selected for these samples where only one or two aqueous species were expected to dominate. Such conditions were identified by equilibrium speciation calculations using the MINTEQA2 and/or MINEQL+ software with the most current, critically reviewed thermodynamic stability constant data of uranyl complexes. These aqueous samples include all the major uranyl-carbonate complexes that may potentially exist under the oxic, neutral to weakly basic conditions commonly encountered at the Hanford Site as well as at selected irrigated agricultural sites. The Hanford pore waters (S01014-55 UFA and S01014-64 UFA) were obtained by high-speed centrifugation of the high-moisture-content samples from the BX-102 core. The chemical composition of similar pore waters has been measured previously.

Fluorescence spectroscopic and lifetime measurements were performed in a cryostat at liquid He-temperature. Briefly, a small volume of the aqueous samples was attached to the cold finger of a cryogenic workstation in which the sample cell was directly exposed to the vapor flow of liquid helium. The fluorescence emission spectra and lifetimes were recorded using a time-gated, intensified charge coupled device (CCD) camera and a photomultiplier tube, respectively.

At room temperature and at the experimental conditions of this work, all the uranyl carbonate complexes showed no discernible fluorescence spectra. Although at elevated uranium concentrations the $UO_2CO_{3(aq)}$ and $Ca_2UO_2(CO_3)_{3(aq)}$ displayed weak but resolved fluorescence spectra. Both the higher complexes, $[UO_2(CO_3)_2^{2-}]$ and $[UO_2(CO_3)_3^{4-}]$ and the mixed carbonate hydroxyl uranyl complex, $[(UO_2)_2\ (OH)_3(CO_3)^-]$ were non-fluorescent even at much higher uranyl concentrations. Lowering sample temperature, all samples showed strong, well-resolved fluorescence spectra at LHeT. To our knowledge, this is the first observation of the fluorescence spectra of these latter complexes.

The di-nuclear complex, $(UO_2)_2(OH)_3(CO_3)^-$, involves the bridging of the two uranyl ions by a hydroxyl and/or a carbonate group and the coordination of both hydroxyl groups and a carbonate in the equatorial plan. Spectral comparison of this complex with those of the other binary uranyl carbonate complexes and uranyl oxyhydroxide minerals suggests that $(UO_2)(OH)_3(CO_3)^-$ bears mostly the spectral signatures of the oxyhydroxide.

The much enhanced spectra resolution allows more accurate calculation of the O=U=O symmetrical stretch frequency, ν_1, that corresponds to the average spacing of the vibronic peaks of the fluorescence spectra. The calculated ν_1 values varied from 864 cm^{-1} for the aqueous uranyl ion to 652 cm^{-1} for $(UO_2)_2(OH)_3(CO_3)^-$. For the three binary uranyl carbonate complexes, the ν_1 values showed gradual decrease from 810 cm^{-1} for $UO_2CO_{3(aq)}$ to 792 cm^{-1} for $[UO_2(CO_3)_3^{4-}]$. Clearly, carbonate complexation caused a decrease of the symmetrical stretching frequency of uranyl. The small ν_1 value for the $(UO_2)_2(OH)_3(CO_3)^-$ complex, once again, indicates a striking structural similarity between this complex and the uranyl oxyhydroxides and some of the uranate salts.

The 55A and 64AB pore waters from the Hanford vadose-zone sediments were non-fluorescent at room temperature. Once the sample temperature was lowered to 6 K, both samples displayed strong, well-resolved uranyl fluorescence spectra. Though the two samples were obtained at 15-foot depth increments beneath Hanford waste storage tank BX-102 tank, their fluorescence spectra are essentially identical, implying similar U(VI) speciation in the pore waters of these sediments.

A comparison of the fluorescence spectral profiles, vibronic peak positions, fluorescence lifetimes, and the symmetric O=U=O stretching frequencies of the sediment pore waters with those of the uranyl carbonate complexes indicates that, while the sediment spectral characteristics generally resembled those of $[UO_2(CO_3)_3^{4-}]$ and $Ca_2UO_2(CO_3)_{3(aq)}$, the best match was found to be the uranyl-tricarbonate complex, $[UO_2(CO_3)_3^{4-}]$. The fluorescence lifetimes, 875 μs and 1153 μs for 55 UFA and 64 UFA, respectively, are slightly longer than that of the $[UO_2(CO_3)_3^{4-}]$. Similarly, the ν_1 values of the pore waters, 807.9 cm^{-1} and 806.3 cm^{-1}, respectively, for 55 UFA and 64 UFA are larger than that of the $[UO_2(CO_3)_3^{4-}]$ complex. These minor variations likely indicate the presence of a small fraction of the $Ca_2UO_2(CO_3)_{3(aq)}$ species. Both the fluorescence lifetimes of the major species, $UO_2(CO_3)_3^{4-}$, and the minor species, $Ca_2UO_2(CO_3)_{3(aq)}$, are so close that the measured values may only represent an weighted average within the error limit of the numerical fittings. These data suggest that the higher U(VI)-carbonate complexes are the mobile species responsible for the subsurface migration of U(VI).

Movement and Dissolution of a Multicomponent, Viscous, Nonaqueous-Phase Liquid in a Fluctuating Water Table System

M Oostrom,[(a)] C Hofstee,[(b)] and TW Wietsma[(c)]

(a) Pacific Northwest National Laboratory, Richland, Washington
(b) Netherlands Institute of Applied Geosciences, TNO-NITG, Utrecht, The Netherlands
(c) W.R. Wiley Environmental Molecular Sciences Laboratory, Richland, Washington

Nonaqueous phase liquids (NAPLs), such as chlorinated solvents and hydrocarbon fuels, are found in the subsurface at many sites. The solubility of NAPLs is usually relatively low and the dissolution is often a kinetic process. As a result, these liquids might form a source of widespread and long-term contamination of groundwater and the presence of NAPLs therefore poses a major environmental problem. Recharge water may come into contact with the liquids and may transport dissolved components downward to aquifers. In addition, dense vapors originating from volatile organic compounds may sink and spread rapidly in the vadose zone. Subsequent partitioning into the groundwater may create extended contaminant plumes. Residual NAPL is likely to be present at several contaminated sites. Carbon tetrachloride is one of the most ubiquitous NAPLs found at U.S. Department of Energy sites. At the Hanford Site in Washington state, an estimated 580 m^3 of a multicomponent NAPL containing carbon tetrachloride was disposed of in several waste sites. The carbon tetrachloride was disposed of with the co-contaminants lard oil, di-butyl-butyl phosphonate (DBBP), and tributyl phosphate (TBP). At present, approximately 65% of the original waste volume has not been accounted for. A better understanding of science issues related to NAPL movement and dissolution is required to aid in the remediation of the Hanford Site.

Typical textbook examples of NAPL sources depict a continuous oil body, submersed in the capillary fringe and below the water table. In cases of past fluctuations of the groundwater table, the oil lens is assumed to overlie a so-called smearing zone, which is characterized by water-entrapped discontinuous lenses. This ideal behavior may be compromised when the NAPL has a viscosity larger than that of water. In addition, most experimental studies on multifluid flow have been limited to single-component NAPLs. We have recently conducted a laboratory experiment to investigate the behavior of a viscous, multicomponent NAPL in a fluctuating water table system and its subsequent dissolution. The experimental work builds on the multifluid flow theory developed in Oostrom and Lenhard (2003), Oostrom et al. (2003), and White et al. (2004).

With respect to the movement of a viscous NAPL, our flow cell experiments have shown that the viscosity differences between the water and the LNAPL are likely to result in entrapment of continuous oil lenses beneath the water table. During the first part of the experiment, a two-dimensional column was packed with sands resembling those that occur in the subsurface at Hanford. Initially, the groundwater was maintained at such a level that the top part of the porous medium is partly saturated. Then a NAPL consisting of DBBP, TBP, and lard oil components was introduced and allowed to redistribute. After static equilibrium was reached, quantitative measurements of NAPL saturations were obtained using the newly constructed, state-of-the-art, dual-energy gamma radiation system located in the W.R. Wiley Environmental Molecular Sciences Laboratory at Pacific Northwest National

Laboratory. Subsequently, the water table was lowered in several steps until a minimum level was reached; then the water table level was gradually increased incrementally. After the original water level was reached, the NAPL was allowed to come to static equilibrium. At that time, the container was scanned again using the gamma system.

In the second part of the experiment, we investigated the mass transfer between the multi-component NAPL source area and the ambient groundwater. This was accomplished by imposing a horizontal groundwater flow in the container. At regular intervals, groundwater samples were extracted from sample ports in the flow cell and analyzed for dissolved organics. The resulting time series of aqueous phase concentrations yielded insight regarding the emission of organic solutes from the source area, which is expected to consist of a combination of discontinuous NAPL droplets and continuous oil lenses. Because a multicomponent LNAPL was used, we were able to study preferential dissolution of the more water-soluble component and the resulting weathering processes of both the oil lens and the discontinuous oil droplets.

Quantitative data obtained during both phases of this experiment will be used to validate two numerical codes: 1) STOMP (White and Oostrom 2004; White et al. 2004) and 2) Modelcode Olie, a TNO-NITG simulator.

References

Oostrom M and RJ Lenhard. 2003. "Carbon Tetrachloride Flow Behavior in Unsaturated Hanford Caliche Material: An Investigation of Residual NAPL." *Vadose Zone Journal* 2:25-33.

Oostrom M, C Hofstee, RJ Lenhard, and TW Wietsma. 2003. "Flow Behavior and Residual Saturation Formation of Injected Carbon Tetrachloride in Unsaturated Heterogeneous Porous Media." *Journal of Contaminant Hydrology* 64:93-112.

White, MD, M Oostrom, and RJ Lenhard. 2004. "A Practical Model for Mobile, Residual, and Entrapped NAPL in Porous Media." *Groundwater* in press.

White, MD and M Oostrom. 2004. *STOMP: Subsurface Transport Over Multiple Phases, Version 3.1. User's Guide.* PNNL-14440. Pacific Northwest National Laboratory, Richland, Washington.

Modification and Decay of Radiation Defects in Tooth Enamel

G Liidja,[(a)] H Kooskora,[(a)] RK Kukkadapu,[(b)] and JE Amonette[(c)]

(a) National Institute of Chemical Physics and Biophysics, Gaithersburg, Maryland

(b) W.R. Wiley Environmental Molecular Sciences Laboratory, Richland, Washington

(c) Pacific Northwest National Laboratory, Richland, Washington

The relative yield and thermal stability of carbonate radicals created by ionizing radiation in bio-apatites, specifically fossil and contemporary tooth enamel, were studied using electron paramagnetic resonance (EPR) spectroscopy. Stepwise heating of powdered enamel samples from room temperature to 245°C was used to simulate aging processes in palaeontological specimens with the goal of refining the EPR dating method.

Tooth samples of two extinct species, a woolly mammoth (*Elephas primigenius*) and a woolly rhinceros (*Rhinoceros antiquitas*), were obtained from the Estonian Natural Museum. Tooth samples from a contemporary African elephant (*Loxodont*) were also obtained from the Tallinn Zoological Garden. The samples were irradiated with doses of 450 Gy and 8 kGy at the Gamma Ray Facility of the Institute of Experimental Biology of the Estonian Agricultural University. Powdered enamel specimens were prepared from the irradiated teeth and preliminary measurements at X-band frequency (ca., 9.2 GHz) were performed at the Estonian National Institute of Chemical Physics and Biophysics. Spectral measurements at Q-band frequency (ca. 35 GHz) were performed on a Bruker ESP 300E spectrometer at the W.R. Environmental Molecular Sciences Laboratory. All spectra were collected at room temperature.

The EPR spectra of irradiated tooth enamel in the vicinity of g=2 consist of overlapping lines and bands originating from CO_2^- radical molecules situated at various bulk positions in the hydroxyapatite crystal lattice and on the surface layer, from other carbonate and sulfate radicals, and from organic components in the enamel (Figure 1). Spectral resolution in the Q-band was sufficient to differentiate and quantitate isotropic CO_2^- molecules tumbling in the hydrated environment of the surface layer (band at H=12105 Gauss, g=2.0009).

The fraction of CO_2^- radicals that were isotropic differed in the irradiated enamel of *Elephas*, *Rhinoceros*, and *Loxodont* (5, 1, and 3 % of all CO_2^- radicals, respectively) grew at the expense of other radicals by as much as 10 to 20% after heating above 200°C, and decayed when heated at temperatures above 225°C. An Arrhenius plot of the isotropic-radical results yielded an activation energy of

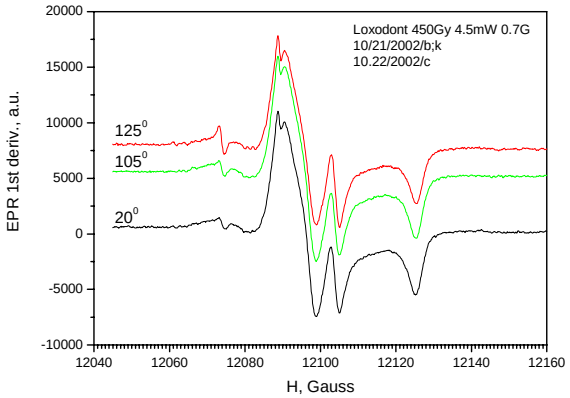

Figure 1. Q-band EPR spectra of irradiated tooth enamel (*Loxodont*) after 0.5-hour heating at the temperatures indicated. Magnetic fields are corrected (gH=24,220 Gauss) and curves are shifted vertically for clarity.

0.24 eV (23 kJ mol^{-1}) and a very small frequency factor, which probably reflects the tunneling character of the underlying process. Based on this activation energy, the time needed to reach thermal equilibrium in buried enamel samples was estimated to be less than 102 years at temperatures near 0°C.

Carbonate radicals in low-symmetry environments (axial and orthorhombic) dominated the EPR spectra. However, the wide asymmetric spectral bands from these radicals were hard to distinguish due to significant overlaps in their features and similarity in their saturation properties. A Monte-Carlo-type spectral simulation revealed orthorhombic (gx=2.0035; gz=2.0022; gy=1.9973) and axial (gx=gz=2.0028, gy=1.9973) radicals coexisting in the unheated powder spectra and their modification into more anisotropic species by heating above 130°C (Figure 2). A narrow spectral line at H=12075 Gauss (g=2.0058), which has been assigned in the literature to sulfate radicals (Vanhaelewyn et al. 2000), also increased with heating above 240°C. This line may be a better candidate for geological dating.

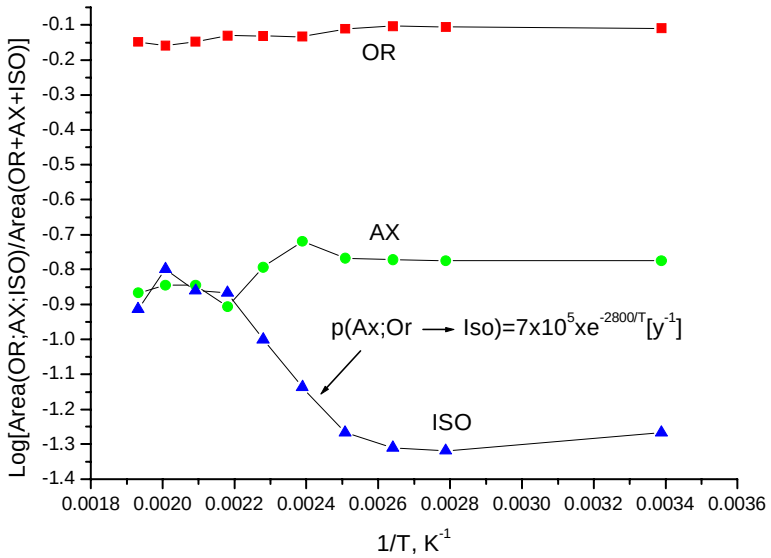

Figure 2. Relative number of carbonate radicals of various symmetry (OR–orthorhombic; AX–axial; ISO–isotropic) in irradiated tooth enamel (*Elephas primigenius*) as a function of preceding heating.

Reference

Vanhaelewyn G, F Callens, and R Grun. 2000. "EPR Spectrum Deconvolution and Dose Assessment of Fossil Tooth Enamel Using Maximum Likelihood Common Factor Analysis." *Applied Radiation and Isotopes* 52:1317-1326.

Towards a More Fundamental Understanding of X-Ray Photoelectron Spectroscopy: A Theoretical and Experimental Approach

ES Ilton[(a)] and PS Bagus[(b)]

(a) Pacific Northwest National Laboratory, Richland, Washington
(b) University of North Texas, Denton, Texas

X-ray photoelectron spectroscopy (XPS) is a frequently used technique for elucidating the chemical state of elements at the near surface of solids. Our ongoing research will advance the scientific community's ability to interpret XP spectra for transition metals and actinides sorbed to or incorporated in environmentally important materials. Specifically, we are coupling a rigorous theoretical approach with experimental data to better determine, among other things, the oxidation state of metals regardless of their structural and chemical environment. Our approach carefully distinguishes inter- and intra-atomic effects. Our initial focus is Cr, in part because it is a major pollutant at various U.S. Department of Energy sites.

We have developed relativistic *ab initio* models for the 3p and 2p spectra of the free Cr^{3+} ion and for the 3p spectrum of the Cr^{3+} ion in an embedded CrO_6 cluster. Theoretical multiplet intensities for the Cr2p lines of the free ion reproduce the main features recorded in XP spectra of Cr_2O_3 (Figure 1), indicating that intra-atomic effects are first order. However, inter-atomic effects are noticeable, particularly for Cr3p. Comparison of *ab initio* models for the Cr3p spectra of an embedded CrO_6 cluster with the free ion model and experimental spectra for Cr_2O_3 demonstrates that the cluster model more closely models the experimental data. The work on condensed-phase effects for the Cr3p XPS of Cr_2O_3 demonstrated that inclusion of the ligand field appreciably improved the comparison of theory with experiment relative to the atomic model (Figure 2) (Bagus et al. 2004). The paper by Ilton et al. (2003) provides a new benchmark for intra-atomic effects in the n*p* XPS of Cr^{3+} ions. In other work, we have identified a new atomic many-body mechanism that makes a major contribution to the complex XPS structure observed for most transition metal atoms.

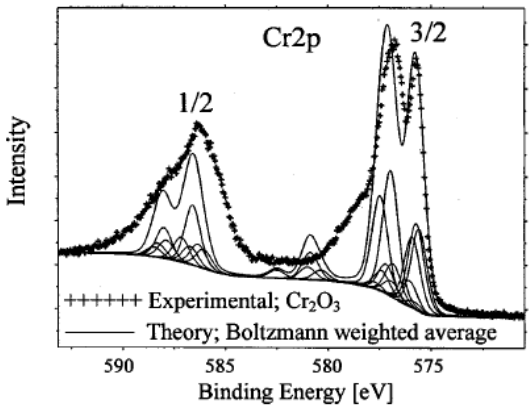

Figure 1. Comparison of theoretical and experimental Cr2p XP spectra of Cr_2O_3.

In the near future, we will develop relativistic models for Cr2p spectra of Cr^{3+} ions in embedded cluster models that represent different coordination environments. In addition, we plan to investigate the influence of bonding environment on the 4f spectra of U ions. This latter work stems from the possibility that U(V) can be stabilized on surfaces during heterogeneous reduction reactions.

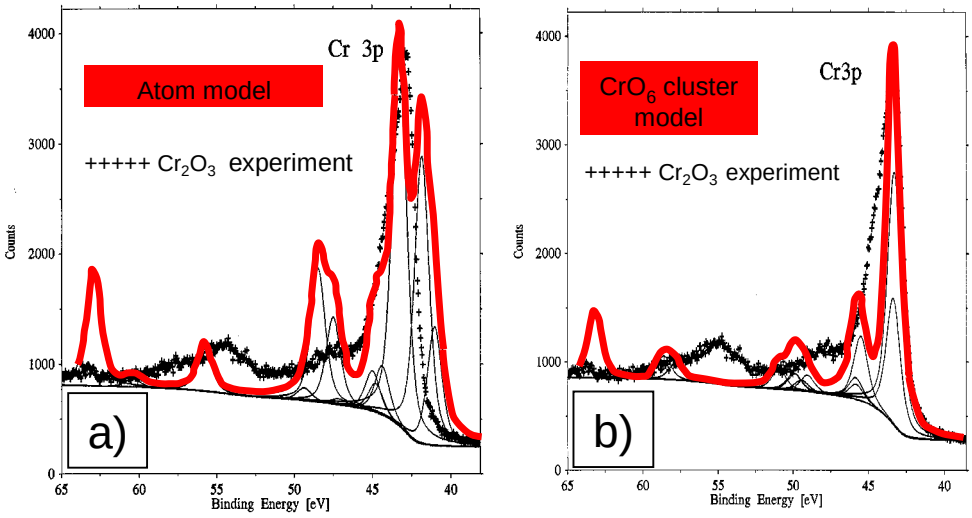

Figure 2. Comparison of theoretical and experimental Cr3p XP spectra of Cr_2O_3 for the atom model (a) and the CrO_6 cluster model (b).

This is both a surprising and potentially important observation that bears on reduction mechanisms for uranyl in natural environments. Theoretical models will help to determine the uniqueness of spectral features for U(IV), U(V), and U(VI) that help to identify U oxidation states.

References

Bagus PS, ES Ilton, and JR Rustad. 2004. "Ligand Field Effects for the 3p Photoelectron Spectra of Cr_2O_3." *Physical Review B* in press.

Ilton ES, W deJong, and PS Bagus. 2003. "Intra-Atomic Many-Body Effects for the P-shell Photo-electron Spectra of the Cr^{3+} Ions." *Physical Review B* 68:125106.

Absolute Mode Assignments of C_6H_6, C_6D_6 and C_6F_6 Using FT-Raman Spectroscopy and *Ab Initio* Methods

SD Williams[(a)] and TJ Johnson[(b)]

(a) Appalachian State University, Boone, North Carolina

(b) Pacific Northwest National Laboratory, Richland, Washington

The absolute vibrational assignments of molecules continue to offer a challenge for both theoretical and experimental physical chemistry. To fully map out the energy surface of molecules, it is important to correctly assign all the fundamental modes of vibration. The power of modern theoretical chemistry brings much to bear on the problem, in particular at calculating the frequencies of the fundamental modes. In the last quarter century computational chemistry has excelled at predicting the absolute frequencies of vibration of many molecules, particularly those of the lighter elements such as hydrocarbons. However, while *ab initio* methods such as executed by the Gaussian software are quite successful at predicting frequencies, the prediction of (relative) band intensities has in general met with limited success.

This is a vibrational study of the homologous series of aromatics, namely benzene, deuterobenzene, and hexafluorobenzene (C_6H_6, C_6D_6, and C_6F_6), which is focused on two main objectives: 1) extending the assignments of these species, particularly hexafluorobenzene, by using Fourier transform Raman spectroscopy to help assess the frequencies and intensities of the modes, along with their polarizations, and 2) extending the capabilities of theoretical methods to predict relative Raman intensities by using a series of single-point calculations of the molecular polarizability for structures that are smoothly displaced along (selected) normal coordinates.

In conventional *ab initio* predictions of Raman activity (as implemented in Gaussian98), the required polarizability derivatives are computed as analytic (Hartree-Fock) or numerical density functional theory (DFT), (MP2) third derivatives of the energy. The assumption underlying this calculation is that the vibrational motion of the molecule can be treated as harmonic. For molecules and vibrational modes with heavy atoms, this assumption may be reasonable, because the amplitude of motion of the atoms is small. With light atom motion (such as H), the harmonic approximation may be poor. A preliminary analysis of our Raman spectra of benzene indicates that the relative intensity of the two totally symmetric (a_{1g}) stretching modes ν_1/ν_2 is 0.89±0.02. (For these molecules, ν_1 is a C-H stretch and ν_2 is a C-C stretch.) Harmonic calculations at the Hartree-Fock level of theory [rhf/6-31(d,p)] predict a ratio of 6.57. This dismal agreement is improved somewhat by DFT and MP2 calculations, but is still quite poor. Because ν_1 is a vibrational mode involving H atoms, it may be expected to be quite anharmonic.

One way to include anharmonic effects in the calculations is to do a series of single-point calculations on molecular structures that are increasingly displaced from the equilibrium geometry along one of the normal coordinates. If the polarizability tensor is computed for each structure, then a simple polynomial fit may be used to estimate the polarizability derivative in a way that does not depend on any assumption of harmonic motion. The pronounced anharmonicity of the ν_1 mode is shown in Figure 1. This result is from the same Hartree-Fock theory described above.

Figure 1 shows the energy as a function of displacement along the ν_1 mode; the red x marks are single-point energies connected by blue line segments, and the green curve is the harmonic parabola that fits the bottom of the curve. The harmonic approximation is clearly good only very close to the equilibrium geometry, but the H atoms sample regions significantly outside of the area where the fit is good. When these single-point calculations are applied to the Raman activities, the relative intensity ratio is much improved; it becomes 1.12 (experimental 0.89). While this is still on the "wrong" side of unity, it is much better than the harmonic prediction. Current computational effort on this problem includes harmonic calculations for C_6F_6 where the increased mass of the F atoms compared to H atoms yields better harmonic results, and extension of the anharmonic calculations to better levels of theory (DFT and MP2).

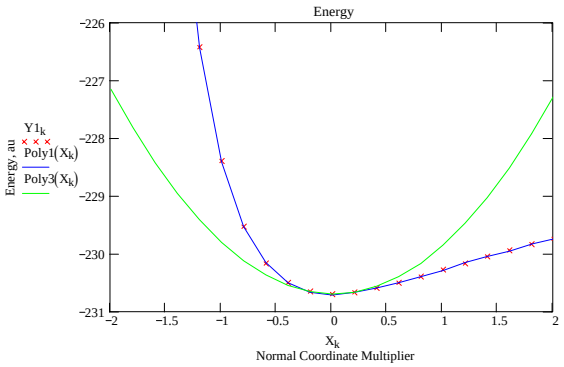

Figure 1. Energy as a function of normal mode coordinate for the ν_1 C-H stretching mode of benzene.

Preliminary experimental results for the case of C_6F_6 can also be seen in Figure 2. In these experiments the Raman-scattered light is analyzed by a Fourier transform spectrometer that has a notch filter installed before the detector to remove the laser excitation line. The Raman spectra are displayed where the abscissa represents the wave-number shift from the laser frequency, in this case the 9394 cm^{-1} excitation from a near-infrared Nd:YAG laser. The ordinate scale is not calibrated into absolute photon flux, but is on the same scale for the two spectra. The two spectra differ in that a calcite analyzer has been placed between the scattered Raman light and the input to the interferometer. In the two spectra, one represents the recorded intensities with the analyzer parallel to the plane of electric field of the excitation laser radiation, and the other with the analyzer perpendicular to the plane. Inspection of Figure 1 shows that the bands at 443 and 370 cm^{-1} are completely depolarized, as their intensities change little depending on the polarizer orientation, while the strong band at 559 cm^{-1} is almost completely extinguished when the polarizer is oriented perpendicular to the electric field of the laser light. The 559-cm^{-1} band is thus a completely symmetric mode and, therefore, is assigned as the a_{1g} symmetric C-F stretch.

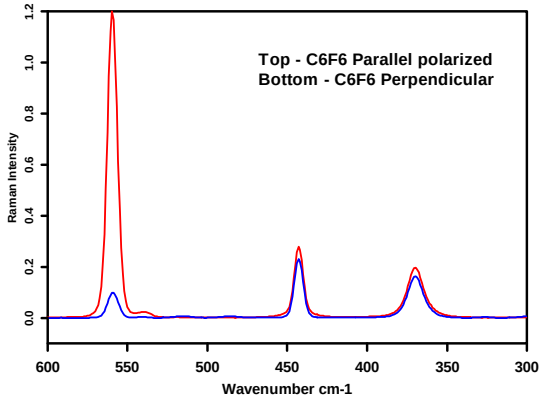

Figure 2. Polarized Raman spectra of C_6F_6 recorded using the analyzer parallel (top trace, in red) and perpendicular (bottom, in blue) to the polarization plane of the excitation laser. The 370- and 443-cm^{-1} bands are depolarized, whereas the band at 559 cm^{-1} is strongly polarized; the 559 band is assigned as the totally symmetric a_{1g} C-F stretching mode.

Further studies on all three of the aromatics, C_6H_6, C_6D_6, and C_6F_6 are planned, including additional polarization studies and theoretical calculations to assign all the Raman active modes.

The Energetics of the Hydrogenolysis, Dehydrohalogenation, and Hydrolysis of 4,4′-Dichlorodiphenyl-trichloroethane from *Ab Initio* Electronic Structure Theory

PG Tratnyek,[(a)] C Zhan,[(b)] EJ Bylaska,[(c)] DA Dixon,[(c)] AR Felmy,[(c)] E Apra,[(d)] and TL Windus[(d)]

(a) Oregon Health and Science University, Portland, Oregon
(b) University of Kentucky, Lexington, Kentucky
(c) Pacific Northwest National Laboratory, Richland, Washington
(d) W.R. Wiley Environmental Molecular Sciences Laboratory, Richland, Washington

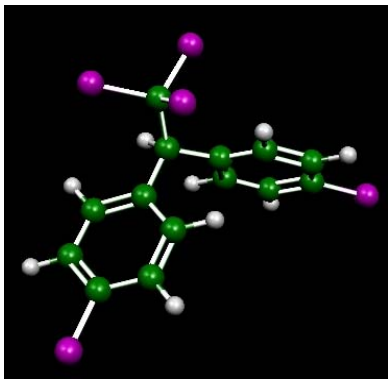

Figure 1. Optimized structure of 4,4′-DDT.

Currently in environmental chemistry, the predominant way for estimating reduction potentials is to use structure activity relationships, such as Benson's group additivity method. These classical methods are known to be reasonably accurate. However, it is difficult to systematically improve the accuracy of a group additivity method because it is difficult for them to explicitly account for neighboring interactions and long-range, through-bond effects. As a consequence, these methods are best used for interpolating properties of a homologous series of molecular species. Another way to estimate reduction potentials is to use *ab initio* methods. *Ab initio* methods do not suffer from the neglect of neighboring interactions and have been shown to be useful for calculating the thermodynamic properties for many types of species.

In this study (Bylaska et al. 2004), electronic structure methods were used to calculate the aqueous reaction energies for hydrogenolysis, dehydrochlorination, and nucleophilic substitution by OH^- of 4,4′-DDT. Thermochemical properties, H^o_f (298.15 K), S^o (298.15 K, 1 bar), ΔG_S (298.15 K, 1 bar) were calculated by using *ab initio* electronic structure calculations, isodesmic reactions schemes, gas-phase entropy estimates, and continuum solvation models for a series of DDT type structures: $(p\text{-}C_6H_4Cl)_2\text{-}CH\text{-}CCl_3$, $(p\text{-}C_6H_4Cl)_2\text{-}CH\text{-}CCl_2^{\bullet}$, $(p\text{-}C_6H_4Cl)_2\text{-}CH\text{-}CHCl_2$, $(p\text{-}C_6H_4Cl)_2\text{-}C{=}CCl_2$, $(p\text{-}C_6H_4Cl)_2\text{-}CH\text{-}CCl_2OH$, $(p\text{-}C_6H_4Cl)_2\text{-}CH\text{-}CCl(=O)$, and $(p\text{-}C_6H_4Cl)_2\text{-}CH\text{-}COOH$. On the basis of these thermochemical estimates, the overall aqueous reaction energetics of hydrogenolysis, dehydrochlorination, and hydrolysis of 4,4′-DDT were estimated. The results of this investigation showed that the dehydrochlorination and hydrolysis reactions have strongly favorable thermodynamics in the standard state, as well as under a wide range of pH conditions. For hydrogenolysis with the reductant aqueous Fe(II), the thermodynamics are strongly dependent on pH, and we found that the stability region of the $(p\text{-}C_6H_4Cl)_2\text{-}CH\text{-}CCl_2^{\bullet}{}_{(aq)}$ species is a key to controlling the reactivity in hydrogenolysis. These results illustrate the use of *ab initio* electronic structure methods to identify the potentially important environmental degradation reactions by calculating the reaction energetics of a potentially large number of organic compounds with aqueous species in natural waters.

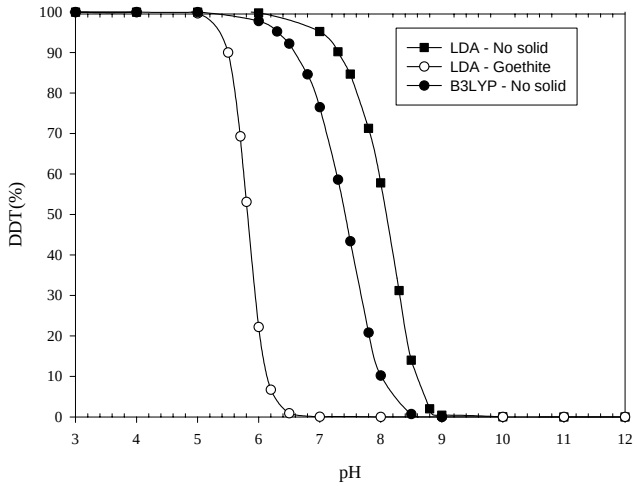

Figure 2. Calculated reduction of 4,4′-DDT for various Fe(II) oxidation reactions.

Reference

Bylaska EJ, DA Dixon, AR Felmy, E Apra, TL Windus, C Zhan, and PG Tratnyek. 2004. "The Energetics of the Hydrogenolysis, Dehydrohalogenation, and Hydrolysis of 4,4'-Dichloro-Diphenyl-Trichloroethane from *Ab Initio* Electronic Structure Theory." *Journal of Physical Chemistry*, in press.

Self-Consistent, Self-Interaction Corrected DFT: The Method and Applications to Extended and Confined Systems

K Tsemekhman,[(a)] EC Brown,[(a)] H Jonsson,[(a)] and EJ Bylaska[(b)]
(a) University of Washington, Seattle, Washington
(b) W.R. Wiley Environmental Molecular Sciences Laboratory, Richland, Washington

We have developed a framework for the self-consistent calculation of self-interaction corrections (SICs) to the density functional theory (DFT) (Tsemekhman et al. 2003a, 2003b). The technique implements the original method due to Perdew and Zunger and combines two procedures: construction of maximally localized Wannier functions (MLWF, procedure due to Marzari and Vanderbilt and to Silvestrelli) and direct minimization of the DFT+SIC total energy functional. In this formulation, the technique is applicable to both confined and extended systems. While construction of the Wannier functions is a useful tool in the case of molecules and clusters, it is a necessary step for extended systems since self-interaction energies constructed on Bloch functions vanish. Construction of Wannier functions thus provides both a good initial guess and a set of functions for which calculation of non-vanishing SICs is possible. Two direct minimization schemes have been used to solve the non-trivial generalized eigenvalue problem. One of the methods that is similar to the Car-Parrinello method uses the gradient proposed by Goedecker and Umrigar (1998). The other method uses a conjugate gradient algorithm with orthogonality constraints that is based upon the work of Edelman et al. (1998).

The DFT+SIC method has been applied to several systems for which standard DFT methods do not work well (Figure 1). One of the more persistent failures of standard DFT methods has been their failure to yield accurate reaction barriers. However, pragmatic approaches in which the exchange correlation functionals are augmented with small amounts of exact exchange have shown great promise (i.e., B3LYP, PBE0, BH&HLYP, and mPWH&HPW91) in improving the accuracy of reaction barriers. Our studies of various chemical reactions showed that SICs can be used in much the same way as exact exchange. Studies of various chemical reactions showed that including a fractional amount of SICs (40%) into a DFT calculation improved the accuracy of calculated reaction energies and barriers considerably.

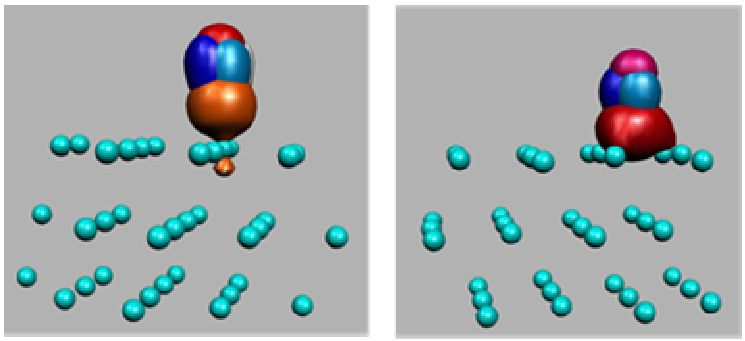

Figure 1. DFT-SIC calculations of the chemisortion of CO on platinum (111). Left: Top coordination site CO orbitals. Right: FCC coordination site CO orbitals.

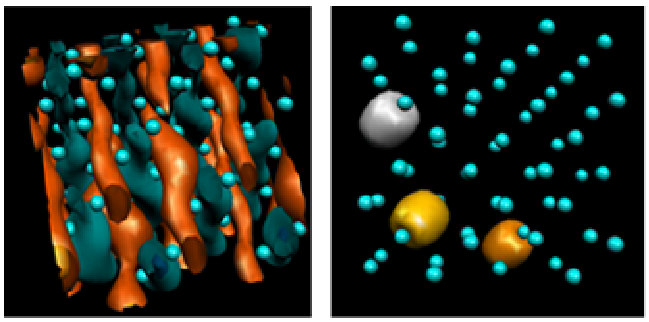

Figure 2. Left: Traditional DFT calculations of Ge predict it to be a metal. The Wannier orbitals are not localized, yet a delocalized metallic state persists. Right: DFT+SIC calculations of Ge predict it to be a semiconductor. The Wannier orbitals are localized and are very similar to Si.

Another notable failure of standard DFT methods has been their inability to reproduce band gaps. For wide-gap systems (insulators and molecules with large highest occupied molecular orbital-lowest unoccupied molecular orbital gaps), SICs appear to work well. DFT+SIC calculations for SiO_2, Al_2O_3, and TiO_2 crystals, as well as for the CO molecule, have shown that 0.4*SIC correction predicts values for the gaps as well as for the singlet-triplet splitting in reasonable agreement with the observed values. However, for systems with narrower gaps, the results are more problematic, and the 0.4*SIC correction appears to overcorrect the DFT results. DFT+0.4*SIC calculations for Si crystal predicted a minimal gap of 2.25 eV compared to the experimental gap of 1.2 eV; in Ge, a 1.2-eV gap is predicted compared to the experimental gap of 0.8 eV.

References

Edelman K, TA Arias, and ST Smith. 1998. "The geometry of algorithms with orthogonality constrants. *SIAM Journal on Matrix Analysis and Applications* 20:303 -353.

Goedecker S and CJ Umrigar. 1998. "Natural Orbital Punctional for the many-electron problem." *Physical Review Letters* 81:866-869.

Tsemekhman K, EJ Bylaska, and H Jonsson. 2003a. "Self-Consistent, Self-Interaction Corrected DFT: The Method and Applications to Extended and Confined Systems." Workshop on *Ab Initio* Electrons Excitations Theory: Towards Systems of Biological Interest, September 21-24, 2003, Donostia International Physics Center, San Sebastian/Donostia, Spain.

Tsemekhman K, EJ Bylaska, EC Brown, and H Jonsson. 2003b. "Self-Consistent, Self-Interaction Corrected DFT: The Method and Applications to Extended and Confined Systems." Poster presented at the 10th edition of the International Congress on the Applications of Density Functional Theory in Chemistry and Physics, September 7-12, 2003, Vrije Universiteit Brussel, Brussels, Belgium.

Influence of Mass Transfer on Precipitation and Dissolution of Uranyl Microprecipitates in Hanford Subsurface Sediments

C Liu,[(a)] JM Zachara,[(a)] JP McKinley,[(a)] and SM Heald[(a,b)]
(a) Pacific Northwest National Laboratory, Richland, Washington
(b) Argonne National Laboratory, Argonne, Illinois

Nuclear waste, spilled onto sediments at the Hanford Site in Washington state, interacted selectively with granitic clasts (plagioclase), forming precipitates of uranyl silicate that occurred almost exclusively in microfractures within the clasts. The uranyl silicate precipitates were found to be discreetly distributed as minute in either radiating or parallel arrays in intraparticle microfractures of a few microns width (Figure 1). Dissolution of the microprecipitates in electrolytes that represented Hanford groundwater was slow and deviated from chemical dissolution kinetics (Liu et al. 2004). These microscopic observations and macroscopic dissolution results suggested the importance of microscopic diffusive mass transport to the uranium removal from flowing waste plumes and concentration within particle grains, and future dissolution and remobilization from the microfractures to groundwater at the site.

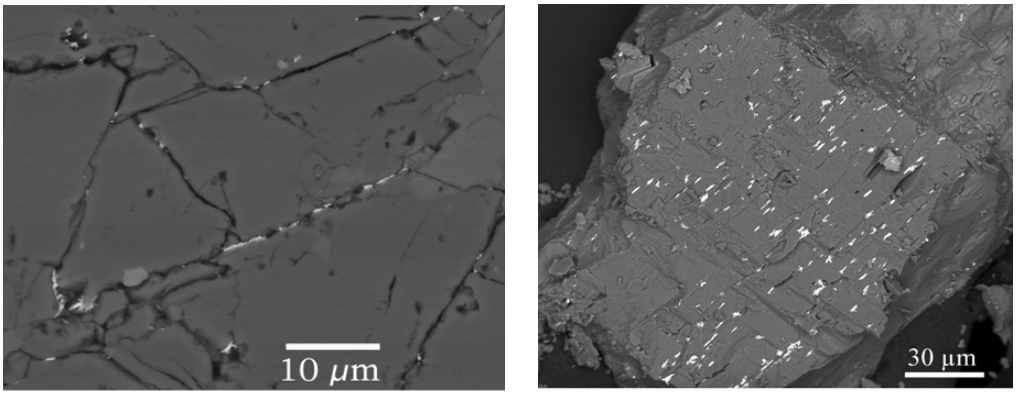

Figure 1. Back-scattered-electron scanning electron microscope images showing intraparticle uranium distribution within a plagioclase feldspar grain. Electron-dense U(VI) precipitates appear white in the images. The left image shows U(VI) crystallites that are aligned in parallel with cleavages on an intraparticle surface that was obtained by pressure-splitting the feldspar grain along a microfracture plane. The right image shows U(VI) precipitates within microfractures in a thin section that was perpendicular to the plane surface in the left image.

Here we developed a microscopic reactive diffusion model to study the influence of mass transfer on uranyl removal from flowing waste plumes and precipitation within plagioclase microfractures, and the dissolution rate and extent of uranyl precipitates in subsurface sediments at Hanford. The key components in the model include coupled diffusion processes of multicomponent ions and ion pairs through electrostatic force, activity coefficient gradients, and equilibrium reactions in the microfractures; reactions of waste-sediment interactions on the intraparticle surfaces of the microfractures during waste intrusion from flowing waste plumes; and chemical reactions of precipitation and dissolution of uranyl precipitates within particle grains.

The model simulation of diffusive waste intrusion into plagioclase microfractures indicated that the mass transfer limitation of Si was the key for the precipitation and concentration of uranyl silicates within particle grains. The calculations showed that the outward diffusion of aqueous Si from intraparticle microfractures to flowing waste plumes was sufficiently compensated from the weathering reactions within the plagioclase microfractures during diffusive waste intrusion that dissolved Si-mineral and supplied aqueous Si. The large ratio of solid surface to aqueous volume within the microfractures led to a fast Si dissolution rate normalized to the aqueous microfracture volume and, thus, maintained a high concentration of aqueous Si within the particle grains. When the inward diffusive flux of U(VI) from the flowing waste plumes was in contact with the high Si concentration within the microfractures, a favorable thermodynamic condition formed for the precipitation and concentration of two uranyl silicates, Na-boltwoodite and uranophane. These two uranyl phases have been identified by various spectroscopic analyses as the most probable candidates of uranyl silicates in the contaminated Hanford sediments, although a unique phase has still not been determined. The calculations also showed that uranyl silicate saturation index increased toward interiors of the plagioclase clasts, a result consistent with the spectroscopic observations that the uranyl precipitates were more abundant within the particle grains than near the particle surfaces.

The simulation of species diffusion and dissolution of the uranyl precipitates from the contaminated sediments indicated that diffusive mass transfer limited the rate of chemical dissolution kinetics within the intraparticle regions. In bicarbonate electrolytes that represent the Hanford groundwater, the dissolution of the uranyl precipitates was promoted by aqueous carbonate species, which formed surface uranyl complexes, detached from uranyl precipitates, and transported out of particle grains (Liu et al. 2004). The calculations showed that the chemical dissolution kinetics that depends on the availability of carbonate species to and removal of uranyl species from the uranyl precipitates in the intraparticle regions was constrained by the diffusive mass transfer processes. Such mass transfer limitation was dependent on the microfracture's connectivity toward particle surfaces, its tortuosity, and steric restriction. Comparing with experimental results, the model calculations indicated that 50 to 95% of the precipitated uranium in the Hanford sediments was associated with the microfractures that were in close contact with the interparticle aqueous phase. The remainder of the uranium was deeply imbedded in particle interiors and exhibited effective diffusivities that were more than three orders of magnitude lower.

Reference

Liu C, JM Zachara, O Qafoku, JP McKinley, SC Heald, and Z Wang. 2004. "Dissolution of Uranyl Microprecipitates from Subsurface Sediments at Hanford Site, USA." *Geochimica Cosmochimica Acta* in press.

Reorganization Energy in Electron Transfer and Its Distance Dependence: Computational Approaches and Illustration for Small Polarons in Iron Oxide

KM Rosso[(a)] and M Dupuis[(a)]
(a) Pacific Northwest National Laboratory, Richland, Washington

In any electron transfer (ET) reaction, the reorganization energy (λ) is an important quantity that controls the ET rate. We recently performed *ab initio* calculations using small clusters to evaluate λ for the transport of conduction electrons in α-Fe_2O_3 (Rosso et al. 2003; Rosso and Dupuis 2004). In that study, we also compared values of λ calculated using two different methods, namely the "direct" and "four-point" methods. Differences in λ that were found between the two approaches were attributed to assumptions built into each method regarding the separability of the reactants in the ET pair. In the current study, we have expanded on this issue by examining in detail the distance dependence of λ for electron transport in iron oxide using large clusters.

We designed a series of *ab initio* calculations on a linear chain of covalently bridged high-spin Fe^{III} atoms. The chain consists of repeating iron octahedra that are linked at octahedral edges (Figure 1). Our computational strategy involved two steps: 1) determine the extent of the structural distortion associated with the creation of a Fe^{II} "defect" at some iron location in the chain, and 2) construct calculations using this distortion to compute the required energetic components of λ as a function of ET distance along the chain. To accomplish the first step, the chain structure was optimized using Crystal98 with one-dimensional periodic

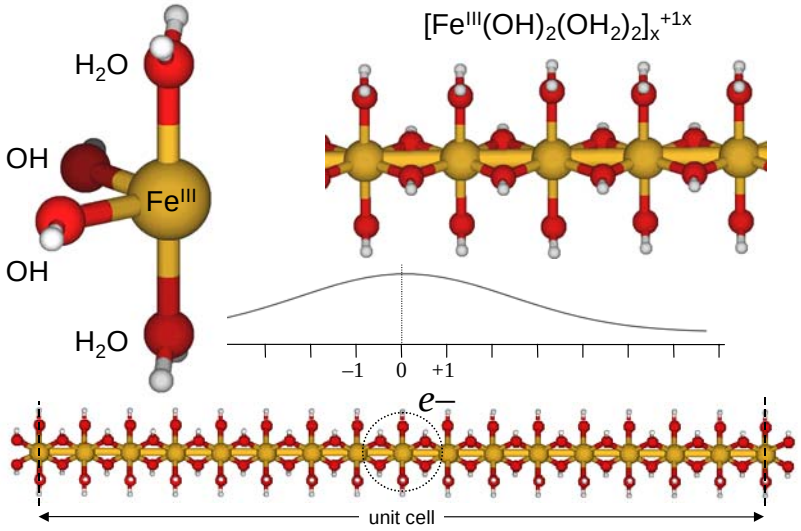

Figure 1. Ball-and-stick models of the Fe repeat unit and the unit cell used for geometry optimizations of the Fe chain. The chain was optimized for the case where all the Fe atoms are in the III oxidation state and for the "defect" case where an "extra" electron has been localized on the central Fe atom, reducing it to the II oxidation state. The "gaussian-like" plot is a conceptualization of the distortion propagating away from the Fe^{II} defect site.

boundary conditions along the chain repeat direction. The size of the distortion accompanying the insertion of an Fe^{II} defect site in the chain was determined by repeating geometry optimizations with increasing supercell sizes, allowing the repeat cell dimension to vary with atomic coordinates. A supercell consisting of 16 repeat units was found to be required to capture the entire distortion (Figure 1), which propagated primarily through the bridging OH groups.

Resulting optimized structures for the Fe^{III}-only chain and the chain containing a single Fe^{II} defect were used for the second step of calculating the energetic components of λ. To do this, we abandoned the periodic boundary condition method and instead used finite cluster representations of the chain. We performed single-point energy calculations to evaluate the quantities above for cases where the electron "hops" anywhere between a nearest-neighbor Fe atom (n=1) to an Fe atom 16 octahedra away (n=16). The calculated distance dependence of λ is shown in Figure 2. The results show that λ varies significantly with ET distance, especially for n ≤ 8. For n > 8, the donor and acceptor Fe atoms are separated by enough distance that there is insignificant coupling between them. Therefore, n > 8 is the condition where the ET reactants become independent of each other. Thus, n=8 is the "size" of one-half of the defect; the total defect size is 16 Fe octahedra. These findings have important implications for our understanding of ET through iron oxide minerals.

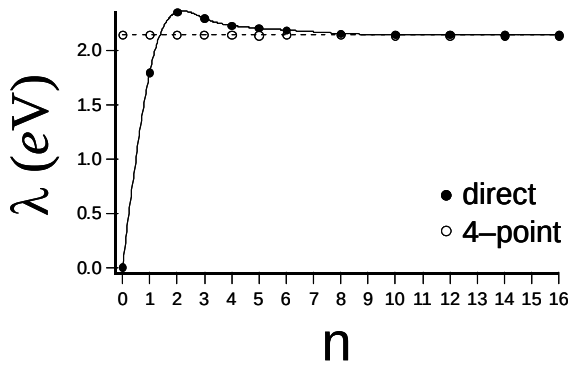

Figure 2. The calculated reorganization energy (λ) as a function of the number of Fe sites (n) spanned in the ET reaction. The "direct" method results, represented by the filled circles, shows that the reorganization energy is sensitive to the ET distance in iron oxide for n ≤ 8.

References

Rosso KM, DA Smith, and M Dupuis. 2003. "An *Ab Initio* Model of Electron Transport in Hematite (α-Fe_2O_3) Basal Planes." *Journal of Chemical Physics* 118:6455.

Rosso KM and M Dupuis. 2004. "Reorganization Energy Associated with Small Polaron Mobility in Iron Oxide." *Journal of Chemical Physics* in press.

Bond-Valence Methods for pKa Prediction: Critical Reanalysis and a New Approach

BR Bickmore,[(a)] CJ Tadanier,[(b)] KM Rosso,[(c)] WD Monn,[(a)] and DL Eggett[(a)]

(a) Brigham Young University, Provo, Utah

(b) Virginia Polytechnic Institute and State University, Blacksburg, Virginia

(c) Pacific Northwest National Laboratory, Richland, Washington

Acid-base reactions are among the most fundamental chemical interactions in natural systems, but the accessibility of these reactions to experimental investigation varies widely. Particularly troubling is the problem of isolating the contribution of specific functional groups on complex solution species and solid surfaces to the total acidity. In the case of solid surfaces, surface complexation models (SCMs) include electrostatic parameters that are usually experimentally inaccessible, along with "intrinsic" acidity constant (pKaint) values for some set of functional groups. A convenient way to reduce the number of fitted parameters in SCMs is to estimate the distribution of sites and surface pKa values theoretically for the different types of functional groups. The most successful and popular of these methods uses "bond valences" to predict pKa value. However, to date this method has not been used to its full potential because only simplified structures that do not account for structural relaxation of solution monomers and solid surfaces have been employed.

In this study, we developed and applied a new approach that is general to solution monomers and solid surfaces. It is based on the use of bond lengths from quantum mechanical calculations and estimates of Me–O bond ionicity. Calculated bond lengths are used to compute bond valences. This approach addresses some of the shortcomings of previous models by explicitly considering 1) realistic metal-oxygen (Me–O) bond lengths rather than idealized ones, and 2) oversimplifications in the treatment of electrostatic considerations in surface complexation models and the interpretation of solution pKa values.

For example, we applied our method to the (001), (100), and (010) faces of the mineral gibbsite [$Al(OH)_3$]. The basal (001) surfaces are populated entirely by $>Al_2OH$ groups, whereas the edge faces have $>Al_2OH$, $>AlOH_2^{+1/2}$, and $>AlOH^{-1/2}$ groups. Predicted pKaint values obtained by our method were reported in Bickmore et al. (2004). For singly coordinated aluminol groups on (100) and (010) faces, predicted pKaint values range from 7.4 to 11.5, with a weighted average of 10.3 assuming equal representation of (100) and (010). pKaint values predicted for the deprotonation of $>Al_2OH_2+$ groups on edge faces range between -0.5 and -2.2. On the basal surface, four of six groups have predicted pKaint values in the range –0.4 to –5.1, one group has a pKaint value of 5.2, and another has a pKaint value of 10.8. Taking into account site densities and observed gibbsite crystal morphologies, this yields a point-of-zero net proton charge of approximately pH 10. It turns out that this picture fits well with the higher-than-expected adsorbed proton densities above the point-of-zero charge observed experimentally. Thus, by incorporating our new pKa predictions into a multi-site surface complexation model, we arrive at an overall description of the surface charging behavior for gibbsite that is consistent with experimental observations. Our approach is the first to do so without having to appeal to extraordinary conditions such as a presence of a large number of defects, ion pairing of H^+ and Cl^- at the surface, or displacement of surface protons by Na^+.

In the development of our model, we found that bond-valence methods for pKa estimation in the past have also neglected other crucial factors as well. First, if the pKa values of solution monomers are to be used to predict pKaint values of surface functional groups, similar electrostatic corrections must be applied in both cases. In surface complexation models, electrostatic corrections are applied by representing a charged surface as a uniform plane of charge density, and an analogous correction can be made to solution monomers by treating them as charged spheres. Second, it must be remembered that real surfaces and real monomers are not homogeneous planes or spheres, respectively. Rather, charge density is distributed rather unevenly, and a further electrostatic correction (which is often fairly large) must be made to account for the proximity of electron density to the point-of-proton attachment. Third, the unsaturated valence of oxygen atoms in oxyacids, hexaquo cations, and oxide surfaces is strongly correlated with acidity after electrostatic corrections are made. However, calculation of unsaturated valence for oxyacids and oxide surfaces must be based on realistic Me–O bond lengths, which in our view can be obtained directly from *ab initio* structure calculations.

Reference

Bickmore BR, CJ Tadanier, KM Rosso, WD Monn, and DL Eggett. 2004. "Bond Valence Methods for pKa Prediction: Critical Reanalysis and a New Approach." *Geochimica et Cosmochimica Acta* in press.

User Projects

Application of Optical Spectroscopy to Interfacial Processes

CC Ainsworth
Pacific Northwest National Laboratory, Richland, Washington

Simulating Mineral Interfaces

JH Weare
University of California San Diego, San Diego, California

Electronic Structure Determination on Mineral Surfaces

KM Rosso
Pacific Northwest National Laboratory, Richland, Washington
U Becker
University of Michigan, Ann Arbor, Michigan

Use of Near Field Scanning Optical Microscopy (NSOM) for Characterization of Surface Properties and Processes Affecting Contaminant Transport in the Vadose Zone

JG Hering
California Institute of Technology, Pasadena, California

The Influence of Clay Minerals on the Formation and Degradation of Geoporphyrins During Diagenesis or Post-Diagenesis

JW Day
U.S. Department of Energy, Richland Operations Office, Richland, Washington

Developing a Parallel Blochl Code

M Valiev
Pacific Northwest National Laboratory, Richland, Washington

Freeze Drying of Iron Oxide Phases

EC Thornton
Pacific Northwest National Laboratory, Richland, Washington

Metal and Radionuclide Bioremediation by Starvation Promoter-Driven Combinatorial Bacteria

A Matin
Stanford University, Palo Alto, California

Characterize Fruit Samples

A Mendoza, TL Stewart
Pacific Northwest National Laboratory, Richland, Washington

Micro-Mineralogical Analysis of Strontium in Biogenic Carbonate Minerals

EE Roden
University of Alabama, Tuscaloosa, Tuscaloosa, Alabama

TV Glass Investigation
A Mendoza
Pacific Northwest National Laboratory, Richland, Washington

Determination of Residual Free Radical Species in Photopolymerized Polyacrylate Thin Films and Composite Layers by ESR
LS Sapochak
Pacific Northwest National Laboratory, Richland, Washington

Simulation of Aqueous Mineral Interfaces, and Development of *Ab Initio* Plane-Wave Methods
A Gramada
University of California, Berkeley, California
M Valiev
Pacific Northwest National Laboratory, Richland, Washington
JH Weare
University of California San Diego, San Diego, California

Use of SEM/TEM for Analysis of MR-1 Biofilms Grown for EMSL NMR Microscopy
BD Wood
Oregon State University, Corvallis, Oregon

AFM Characterization of Self-Assembled Heterogenite Particles
RL Penn
University of Minnesota, Minneapolis, Minnesota

Infrared Spectral Features and their Relationship to Glass Dissolution Behavior
M Bliss
Pacific Northwest National Laboratory, Richland, Washington

Effects of Impermeable-Zone Diffusion on Continuous and Intermittent Pump-and-Treat Remediation at Dover AFB – Model Simulation and Field Results
WP Ball
Johns Hopkins University, Baltimore, Maryland

EPR Studies of Cu Sorption on Clay Minerals
DG Strawn
University of Idaho, Moscow, Idaho

Basic Energy Science
J Chang
Pacific Northwest National Laboratory, Richland, Washington

TEM Image of Mesoporous Silica
BM Jeong
Pacific Northwest National Laboratory, Richland, Washington

Distribution and Occurrence of Pb-Phosphates in *B. Cepacia* Biofilms
AS Templeton, AM Spormann, GE Brown
Stanford University, Palo Alto, California

An Electrochemical Investigation of the Enhanced Reactivity of Clays in Contact with Iron Metal
BA Balko, AB Clark
Lewis and Clark College, Portland, Oregon

Quantitative Measurements in Scattering Media: Path length Determination of Short Wavelength Near Infrared Light in Fish Tissue
AG Cavinato, SP Nord, RA Tache
Eastern Oregon University, La Grande, Oregon
M Lin, B Rasco
Washington State University, Pullman, Washington

Oxygen Versus Iron Terminations in Hematite Basal Surfaces: STM Imaging in Air and in Aqueous Solutions
AG Stack
University of California Davis, Davis, California

Resonance Raman Spectroscopy of Dyes Used as Solar Energy Sensitizers
JL McHale, MY Choi, MA Webb
University of Idaho, Moscow, Idaho

Mechanisms of Fe Biomineralization Induced By Dissimilatory Iron Reduction
CM Hansel, S Fendorf
Stanford University, Palo Alto, California

Mineralogical Analysis of Substrates and End-Products of Microbial Fe Redox Transformations
EE Roden
University of Alabama, Tuscaloosa, Tuscaloosa, Alabama

Modification and Decay of Radiation Defects in Tooth Enamel
G Liidja
National Institute of Chemical Physics and Biophysics, Gaithersburg, Maryland

Solid Phase Characterization/Speciation of U in 300 Area Sediments-Hanford
RJ Serne
Pacific Northwest National Laboratory, Richland, Washington

Contaminant-Organic Complexes: Their Structure and Energetics in Surface Decontamination Processes

CL Barajas
Ohio State University, Columbus, Ohio
SJ Traina
University of California Merced, Merced, California
NP Qafoku, CC Ainsworth
Pacific Northwest National Laboratory, Richland, Washington

Dissolution and Precipitation in the Hanford Sediments Under Hyperalkaline Conditions

NP Qafoku
Pacific Northwest National Laboratory, Richland, Washington

Time Resolved Study of Photoluminescence from Gold Nanostructures

MR Beversluis, L Novotny
University of Rochester, Rochester, New York

Analysis of Clays Reacted with Simulated Hanford Tank Waste

S Choi, JD Chorover
University of Arizona, Tucson, Arizona

Analysis of Iron Mineralogy of Clay Sediments Exposed to Reducing Conditions

DC Cooper
Idaho National Engineering and Environmental Laboratory, Idaho Falls, Idaho

Microbial Reduction of Iron in Sedimentary Clays: Implications for Subsurface Microbial Ecology and Bioremediation

H Dong
Miami University, Miami, Florida

Formulating the CD-MUSIC Surface Complexation Model from First Principles Calculations for Phosphate Adsorption on Goethite

CJ Tadanier
Virginia Polytechnic Institute, Blacksburg, Virginia

Analyses of Electron Density Distributions in Earth Materials with Implications for Reactivity

GV Gibbs
Virginia Polytechnic Institute, Blacksburg, Virginia

Surface Structure Effects on Direct Reduction of Iron Oxides by *Shewanella oneidensis*

AL Neal
University of Georgia, Athens, Georgia

Structure and Reactivity of the Basal and Edge Surfaces of Gibbsite
KM Rosso
Pacific Northwest National Laboratory, Richland, Washington
B Bickmore
Brigham Young University, Provo, Utah

Environmental Technology Division Laboratory Directed Research & Development Project for Uranium Sensor Test
W Yantasee
Pacific Northwest National Laboratory, Richland, Washington

The Role of Algae and Bacteria from Berkeley Pit Lake in Metal Sorption Processes
D Bocioaga, GG Mitman
University of Montana, Missoula, Montana

Outer-Sphere Electron Transfer Kinetics of Metal Ion Oxidation by Molecular Oxygen
JJ Morgan
California Institute of Technology, Pasadena, California

Critical Point Properties of Electron Density Distributions in High Pressure Mineral Phases
N Ross
Virginia Polytechnic Institute, Blacksburg, Virginia

Biogenic Iron Mineralization by a Novel Gram-Positive Bacterium: Impact on the Fate of 2,4,6-Trinitrotoluene
T Borch, WP Inskeep
Montana State University, Bozeman, Montana

Pressure Effect on Electronic Structure of Anthracene Single Crystals: Formation and Modification of Structural Defects
ZA Dreger, YM Gupta
Washington State University, Pullman, Washington

IC Identification of By-Products in Biomass Pyrrolidone Chemistry
JE Holladay
Pacific Northwest National Laboratory, Richland, Washington

Infrared Detection of Organics in Artificial Aging Experiments
CJ Thompson
Pacific Northwest National Laboratory, Richland, Washington

Characterization of Diesel Soot Material by Using IR and Raman Spectroscopy
DH Kim
Pacific Northwest National Laboratory, Richland, Washington

Gas Chromatography of Solvent Extracted Organo-Phosphorous Compounds from Soils

TA Blake, PL Gassman
W.R. Wiley Environmental Molecular Sciences Laboratory, Richland, Washington

HPLC Analysis of Humic Monomers and Polymers

JE Amonette, CK Russell
Pacific Northwest National Laboratory, Richland, Washington

Analysis of CCl_4 and its Degradation Products by Gas Chromatography

JE Amonette
Pacific Northwest National Laboratory, Richland, Washington

The Chemistry and Mineralogy of Variable Charge Soils

NP Qafoku
Pacific Northwest National Laboratory, Richland, Washington

Iron Mineral and Chromium Reduction by *Cellulomonas* Subspecies

R Gerlach, T Borch
Montana State University, Bozeman, Montana

Investigation into the Polarized Raman Spectra of Benzene, Benzene-d6 and Hexafluorobenzene

SD Williams
Appalachian State University, Boone, North Carolina

Measure Fluorescence Spectra from LiF Film

MK Murphy
Pacific Northwest National Laboratory, Richland, Washington

Highly Selective Monolayer Sorbents for Advanced Analytical Applications

RS Addleman
Pacific Northwest National Laboratory, Richland, Washington
JT Bays
U.S. Military Academy, West Point, New York

Isolation of Isotopically Labeled Nucleic Acids

K McAteer
Washington State University, Pullman, Washington
NG Isern
W.R. Wiley Environmental Molecular Sciences Laboratory, Richland, Washington

The Characterization of the $SiC/SiO_2/C$ Composite

H Zhang, L Wang
Washington State University, Pullman, Washington

Separation and Measurement of DNA from Soil Extracts
RM Ozanich, A Dagan
Pacific Northwest National Laboratory, Richland, Washington

Multi-Resolution Structure and Reactivity of Kinetically Roughened Oxide Surfaces: Nanometric Scaling Behavior and Molecular-Scale Controls
KM Rosso, EJ Bylaska
Pacific Northwest National Laboratory, Richland, Washington
P Meakin
Idaho National Engineering and Environmental Laboratory, Idaho Falls, Idaho

The Development of Thermodynamic Models for Actinide Species in Mixed Solvent Systems: Application to Binding in Microbial Membranes
SB Clark
Washington State University, Pullman, Washington

CASMGS Consortium
JE Amonette
Pacific Northwest National Laboratory, Richland, Washington

Center for Research on Carbon Sequestration
JE Amonette
Pacific Northwest National Laboratory, Richland, Washington

Sensor and Tracer Technology for Characterization of Ultra-Low CO_2 Leakage Fluxes
JE Amonette, JL Barr
Pacific Northwest National Laboratory, Richland, Washington

Model Porous Solids and Sediments
JE Amonette
Pacific Northwest National Laboratory, Richland, Washington

Biogeochemistry of Uranium Under Reducing and Re-oxidizing
JE Amonette
Pacific Northwest National Laboratory, Richland, Washington

Enhancing Carbon Sequestration and Reclamation of Degraded Lands and Sequester C in Soils
JE Amonette
Pacific Northwest National Laboratory, Richland, Washington

Array-Based Photoacoustic Spectroscopy
JE Amonette, TS Autrey, JL Barr
Pacific Northwest National Laboratory, Richland, Washington

Carbon Tetrachloride Degradation Reaction Mechanisms
JE Amonette, EJ Bylaska
Pacific Northwest National Laboratory, Richland, Washington
PG Tratnyek
Oregon Health Sciences University/Oregon Graduate Institute, Portland, Oregon

EPA Consulting: MNA of Inorganic Contaminants in Groundwater
JE Amonette
Pacific Northwest National Laboratory, Richland, Washington

A Bioengineering Approach to the Production of Metal and Metal Oxide Nanoparticles
DR Strongin
Temple University, Philadelphia, Pennsylvania

Chemical Speciation of Americium, Curium, and Selected Tetravalent Actinides in High-Level Waste
AR Felmy, Z Wang, OS Qafoku
Pacific Northwest National Laboratory, Richland, Washington

Influence of Reactive Transport on the Reduction of U(VI) in the Presence of Fe(III) and Nitrate
C Liu
Pacific Northwest National Laboratory, Richland, Washington

Interactions Between Fe(III) – Reducing Bacteria and Fe Oxides: Microbial and Geochemical Dissolution Controls
ES Ilton, JM Zachara, KM Rosso
Pacific Northwest National Laboratory, Richland, Washington

Coupling of Fe and Tc Speciation in Subsurface Sediments: Implications to Long-Term Tc Immobilization
JM Zachara
Pacific Northwest National Laboratory, Richland, Washington

Mineralogic Residence and Desorption Rates of Sorbed ^{90}Sr in Contaminated Subsurface Sediments: Implications to Future Behavior and In-Ground Stability
JM Zachara
Pacific Northwest National Laboratory, Richland, Washington

Impacts of Mineralogy and Competing Microbial Respiration Pathways on the Fate of Uranium in Contaminated Groundwater
JM Zachara
Pacific Northwest National Laboratory, Richland, Washington

Characterization of U(VI) Sorption-Desorption Processes and Model Upscaling
JM Zachara
Pacific Northwest National Laboratory, Richland, Washington

The Influence of Calcium Carbonate Grain Coatings on Contaminant Reactivity in Vadose Zone
JM Zachara
Pacific Northwest National Laboratory, Richland, Washington

Science and Technology Road Mapping for Needs From All Sources
JM Zachara
Pacific Northwest National Laboratory, Richland, Washington

Hanford GW/VZ Science Integration
JM Zachara
Pacific Northwest National Laboratory, Richland, Washington

Influence of Mass transfer on Bioavailability and Kinetic Rate of U(VI) Biotransformation
C Liu, Z Wang, Z Zachara
Pacific Northwest National Laboratory, Richland, Washington

Reactions and Transport of Toxic Metals in Rock Forming Silicates at 25°C
ES Ilton
Pacific Northwest National Laboratory, Richland, Washington

Actinide Interactions with Environmental Bacteria
MP Neu
Los Alamos National Laboratory, Los Alamos, New Mexico

Characterization of U(VI) Speciation in Samples from Laboratory Batch and Column Experiments
J Wan
Lawrence Berkeley National Laboratory, University of California, Berkeley, Berkeley, California

Liquid Infrared Spectroscopy and Spill Phenomenology
PL Gassman
W.R. Wiley Environmental Molecular Sciences Laboratory, Richland, Washington
RS Disselkamp, JL Hylden
Pacific Northwest National Laboratory, Richland, Washington

Mechanisms and Kinetics of Organic Aging in High-Level Nuclear Waste
TS Autrey, DM Camaioni
Pacific Northwest National Laboratory, Richland, Washington

Movement and Dissolution of a Viscous, Multicomponent Light Nonaqueous-Phase Liquid in a Fluctuating Water Table System

C Hofstee
Netherlands Organization for Applied Scientific Research TNO-NITG, Utrecht, Netherlands

Quantification and Chemical Analysis of Iron Oxidation in Microbially-Reduced Sediments

J Komlos, PR Jaffe
Princeton University, Princeton, New Jersey

Model Development on Using Clay Membranes for Arsenic Removal from Drinking Water

B Deng
University of Missouri, Columbia, Missouri

Multiple Sensor Data Integration

NB Valentine, KH Jarman
Pacific Northwest National Laboratory, Richland, Washington

Biogeochemical Heterogeneity in the Subsurface

T Resch, PE Long
Pacific Northwest National Laboratory, Richland, Washington

Intermediate Flow Cells

T Resch, JE Szecsody
Pacific Northwest National Laboratory, Richland, Washington

Computational Investigation of Acid Base, Surface Complexation, and Oxidation/Reduction Reaction Mechanisms on Iron Oxide and Silicate Surfaces

JR Rustad
University of California, Berkeley, California
AR Felmy
Pacific Northwest National Laboratory, Richland, Washington

The Kinetics of Direct Enzymatic Reduction of Uranium (VI): Effects of Ligand Complexation and U(VI) Speciation

CC Ainsworth, KB Wagnon, Z Wang
Pacific Northwest National Laboratory, Richland, Washington

Staff

Nancy S. Foster-Mills, Senior Research Scientist, Technical Lead
(509) 376-1343, nancy.foster@pnl.gov

Cheryl E. Hall, Administrative Secretary
(509) 376-5362, cheryl.hall@pnl.gov

Paul L. Gassman, Research Scientist
(509) 376-7972, pl.gassman@pnl.gov

Ravi Kukkadapu, Senior Research Scientist
(509) 376-3795, ravi.kukkadapu@pnl.gov

Thomas W. Wietsma, Research Scientist
(509) 376-6588, wietsma@pnl.gov